Completion of a SCUBA survey of Lynds dark clouds and implications for low-mass star formation

Anja E. Visser, John S. Richer

Mullard Radio Astronomy Observatory, Cavendish Laboratory, Madingley Road, Cambridge CB3 0HE, United Kingdom

anja.visser@wanadoo.nl, jsr@mrao.cam.ac.uk

and

Claire J. Chandler

National Radio Astronomy Observatory, PO Box O, Socorro, NM 87801, USA

cchandle@nrao.edu

ABSTRACT

We have carried out a survey of optically selected dark clouds using the bolometer array SCUBA on the James Clerk Maxwell Telescope at $\lambda = 850\ \mu$m. The survey covers a total of 0.5 square degrees and is unbiased with reference to cloud size, star formation activity, and the presence of infrared emission. Several new protostars and starless cores have been discovered; the protostars are confirmed through the detection of their accompanying outflows in CO(2–1) emission. The survey is believed to be complete for Class 0 and Class I protostars, and yields two important results regarding the lifetimes of these phases. First, the ratio of Class 0 to Class I protostars in the sample is roughly unity, very different from the 1:10 ratio that has previously been observed for the ρ Ophiuchi star-forming region. Assuming star formation to be a homogeneous process in the dark clouds, this implies that the Class 0 lifetime is similar to the Class I phase, which from infrared surveys has been established to be $\sim 2 \times 10^5$ yr. It also suggests there is no rapid initial accretion phase in Class 0 objects. A burst of triggered star formation some $\sim 10^5$ yr ago can explain the earlier results for ρ Ophiuchus. Second, the number of starless cores is approximately twice that of the total number of protostars, indicating a starless core lifetime of $\sim 8 \times 10^5$ yr. These starless cores are therefore very short lived, surviving only two or three free-fall times. This result suggests that, on size scales of $\sim 10^4$ AU at least, the dynamical evolution of starless cores is probably not controlled by magnetic processes.

Subject headings: ISM: clouds — stars: formation — stars: pre-main-sequence

1. Introduction

Systematic surveys of the earliest stages of low-mass star formation provide vital information on the physics of cloud collapse. In particular, if complete samples of protostars and pre-stellar cores can be identified, their relative lifetimes can be estimated, if it is assumed that the clouds are not being observed at a special time in their evolution. Such studies are vital for differentiating between models of star formation, which can predict very different protostellar accretion histories. In some models, the evolution of molecular cloud cores is controlled entirely by strong magnetic fields, leading to lifetimes determined by the ambipolar diffusion timescale, which is typically 10^7 yr (Ciolek & Mouschovias 1994). However, recent three-dimensional numerical simulations of turbulent, gravitationally unstable clouds show that cores can form and evolve over only a few dynamical timescales, even if significant magnetic fields are present (Li et al. 2000; Heitsch, Mac Low, & Klessen 2001). For typical cloud conditions, this implies evolution on timescales of about 10^6 yr.

Once a gravitationally unstable core has formed and started to collapse, the accretion rate of the protostar is governed by the initial conditions at the onset of collapse. The idealized collapse of a singular isothermal sphere (Shu 1977) proceeds with a uniform accretion rate. Other accretion models starting from different initial conditions predict a short phase of rapid accretion, succeeded by a more or less constant accretion rate (e.g., Foster & Chevalier 1993; McLaughlin & Pudritz 1997). If evolutionary phases of different accretion rates can be identified observationally, then their relative lifetimes can then be estimated, possibly enabling the discrimination between these different models.

Complete surveys of infrared protostars have been used to obtain good estimates for the lifetime of infrared protostars, in particular the Class I, II, and III phases of protostellar evolution. From such surveys, Wilking, Lada, & Young (1989) and Kenyon et al. (1990) conclude that the Class I phase lasts $\sim 2 \times 10^5$ yr in the low-mass, star-forming regions of ρ Ophiuchus and Taurus, and this lifetime is consistent with typical cloud collapse models (e.g., Adams, Lada, & Shu 1987). However, the timescales associated with the earlier phases of star formation, specifically the Class 0 phase (André et, Ward-Thompson, & Barsony 1993) and the precollapse phase (Ward-Thompson et al. 1994), are much more uncertain. Most samples of dense cores derive originally from catalogs of optically selected dark clouds, which were subsequently searched for associated *IRAS* emission (e.g., Beichman et al. 1986; Clemens & Barvainis 1988; Benson & Myers 1989; Lee & Myers 1999; Jijina, Myers, & Adams 1999). Since Class 0 protostars are typically too cold and faint to have been detected by *IRAS*, complete samples of both Class 0 protostars and truly "starless" cores (as opposed to cores lacking an associated *IRAS* source or 2 μm emission) have been difficult to obtain. In one of the few regions where complete samples of Class 0 and Class I objects exist — the ρ Ophiuchi cloud — the results imply that the Class 0 phase lasts only one-tenth of the Class I phase in this region, i.e., 2×10^4 yr (André & Montmerle 1994). However, there are few, if any, good statistical constraints in other regions of star formation.

The advent of large bolometer arrays on millimeter and submillimeter telescopes has made the first systematic surveys for the earliest phases of star formation possible. Typical observing wavelengths, $\lambda \sim 0.5$ to 1 mm, lie towards the Rayleigh-Jeans side of the Planck function for all reasonable dust temperatures

$T \gtrsim 7$ K. Millimeter and submillimeter dust emission is therefore an excellent tracer of the youngest embedded protostars and starless dense cores, which are regions of high dust column density that can be too cold for detection by far-infrared instruments. In this paper, we present the second and concluding part of a survey, using the submillimeter camera SCUBA on the James Clerk Maxwell Telescope (JCMT), of dust continuum emission from typical, nearby, molecular clouds forming low-mass stars. The observations are sufficiently sensitive to detect all the embedded protostars and starless cores above a certain mass limit, and so allow us to estimate the lifetimes of these earliest phases of star formation. In an earlier paper (Visser, Richer, & Chandler 2001, hereafter Paper I) we presented initial results derived from images of the smaller clouds in the sample. Here we include the images of the larger clouds and, using the full survey, present a detailed analysis of the structure of the cores, their star forming properties, and the properties of their molecular outflows. We also estimate the relative and absolute lifetimes of the various prestellar and protostellar phases based on their detection rates.

2. Source sample

The clouds observed were selected from those listed as opacity class 6 in the Lynds catalog of dark nebulae, which contains 1802 optically dark clouds selected from the POSS plates (Lynds 1962). Lynds cataloged the clouds by eye based on their apparent opacity, using an arbitrary scale of 1 to 6, with the class 6 clouds being the most opaque ($A_V \gtrsim 10$ mag). These estimates were based on a comparison of the cloud with a neighboring field on the POSS plate, and the classification is therefore somewhat subjective. The Lynds catalog contains a total of 147 opacity class 6 clouds covering a total area of ~ 2 deg^2, with individual clouds having a mean minor axis of $4'$ and major axis of $11'$. Some of these clouds are small and round, like globules, but others are extended and filamentary. The optical appearance of most clouds is quiescent, with only a small fraction of the clouds looking shocked.

Star formation in Lynds class 6 clouds has been studied by Parker (1991) following a reanalysis of their positions (Parker 1988) and an investigation of their association with *IRAS* sources. However, the selection criteria he used based on *IRAS* detections failed to find the well-known Class 0 source B335 (L663) (Parker 1989), demonstrating the importance of understanding the selection effects introduced by such wavelength-dependent criteria. Our optical selection criterion corresponds to a limiting column density, and is biased towards finding nearby clouds.

Forty-two opacity class 6 clouds were selected from the Lynds catalog with sizes and positions determined by the observing time allocated and observing mode available at the JCMT (see § 3 below). This resulted in an essentially random selection of clouds. The first to be observed were the small or filamentary clouds that could be mapped using the single SCUBA field of view, before the commissioning of large-area (scan) mapping. These results are presented in Paper I. The larger clouds were mapped when scan mapping became available. Because of the local sidereal time ranges allocated to the observations, we were able to map several areas in ρ Ophiuchus, and more than one-third of all the clouds are part of the ρ Ophiuchi cloud complex. The full sample contains no biases relating to size, star formation activity, or the presence of infrared emission, and so is statistically representative of nearby, dark clouds. The names and positions of all the clouds surveyed are given in Table 1, along with identifications from the Barnard (1927) catalog (B) and the Clemens & Barvainis (1988) catalog (CB).

2.1. Distances

The distances to nearby clouds can be difficult to determine because neither star counts nor kinematic determinations are very reliable. The use of foreground star counts requires a precise knowledge of the distribution of the stars in the direction of the cloud, and the cloud needs to be large to make the count statistically relevant. The LSR velocity of the cloud is usually influenced by local motions and cannot, on its own, be used to determine the distance toward the cloud. Nevertheless, to be able to obtain physical parameters from the data, the correct distances need to be known. Here we use the method of associating the dark clouds with larger molecular cloud complexes (see, e.g., Launhardt & Henning 1997). Fifteen of our clouds have distances previously reported in the literature (Hilton & Lahulla 1995) with which our distance estimates agree very well. A discussion of the distances for the clouds presented in Paper I is given in an appendix to that paper. For the larger clouds that were scan mapped details are given by Visser (2000). The assumed distances and associated cloud complexes are summarized in Table 1.

2.2. *IRAS* sources

Table 2 lists the *IRAS* sources in the Point Source Catalogue (PSC) associated with the Lynds clouds in our sample. Association is defined to be all *IRAS* PSC sources within the SCUBA maps, and the *IRAS* sources that were associated with the clouds by Parker (1988). Most of the *IRAS* sources in Table 2 had already been associated with the Lynds clouds by Parker. Five *IRAS* sources covered by the SCUBA maps were not associated by Parker (even though they sometimes satisfy Parker's selection criteria, for example IRAS 19186+2325 in L771), and these are marked with a "d." Sources associated with the cloud by Parker, but not covered by the maps, are marked with a "b." The eight candidate protostars in common with those selected and studied by Parker (1991) are indicated with a "c."

Information about the nature of some of these *IRAS* sources is available in the literature and is included in Table 2. IRAS 16445−1352 is probably cirrus of the type very common in ρ Ophiuchus, since it is only detected at 60 and 100 μm and is extended at both wavelengths (Beichman et al. 1986). IRAS 16455−1405[1] is listed as a Class I source by Bontemps et al. (1996). An outflow was not detected, however, and the source was identified by Parker (1991) as a T Tauri star with an optical counterpart. This source is not covered by the SCUBA map and is not discussed further. T Tauri stars covered by this survey are IRAS 16459−1411 (André & Montmerle 1994) and IRAS 19181+1056, which is associated with HH 32 (Curiel et al. 1997). *IRAS* sources 16442−0930, 18148−0440, 19345+0727, 23238+7401, and 16285−2355 are all known protostars

[1]mistyped as 16445−1405 by Bontemps et al. (1996)

with outflows partly mapped by Bontemps et al. (1996). IRAS 19184+1055 is identified as an OH/IR star by Chengalur et al. (1993), and 16285−2358 is an optically visible star (Ichikawa & Nishida 1989).

IRAS 22051+5848 is a protostar with an outflow presented by Parker, Padman, & Scott (1991). Launhardt, Ward-Thompson, & Henning (1997) suggest that IRAS 23228+6320 is a protostar, but an outflow is not detected (Parker et al. 1991). Massive outflows are detected from IRAS 21017+6742 (Myers et al. 1988) and from the vicinity of 19180+1116 and 19180+1114 (Armstrong & Winnewisser 1989). Anglada, Sepulveda, & Gomez (1997) argue that of these latter two it is more likely that 19180+1114 drives the outflow, taking into account ammonia emission, their spectral energy distributions (SEDs), and the location of the sources with respect to the CO flow. Identifications from the literature are listed in column (7) of Table 2.

In general, field stars and T Tauri stars are detected in the 12 and 25 μm *IRAS* bands with their SEDs rising towards shorter wavelengths, while embedded protostars (and cirrus clouds) are detected at 60 and 100 μm with SEDs rising toward longer wavelengths. This trend is seen in the sample presented in Table 2, although many of the *IRAS* fluxes are high upper limits owing to confusion.

3. Submillimeter continuum observations and data reduction

Observations were made using the submillimeter camera, SCUBA, on the 15 m JCMT on Mauna Kea, Hawaii (Holland et al. 1999). SCUBA comprises two arrays of bolometer detectors, which can be used simultaneously by means of a dichroic beam splitter. The arrays are cooled to a temperature of 0.1 K to achieve high sensitivity. The 37 bolometers of the long-wavelength array are optimized for observations at 850 μm, and the 91 bolometers of the short-wavelength array are optimized for operation at 450 μm. The diffraction-limited FWHM beam sizes at these two wavelengths are $14''$ and $8''$, respectively. At 850 μm, the beam is well approximated by a single Gaussian, but at 450 μm there is an extended error beam containing a roughly equal amount of power to the main diffraction beam, spread over a diameter of approximately $40''$. Most of the conclusions in this paper are therefore based on the 850 μm data.

The bolometers form a hexagonal pattern and are spaced approximately two beamwidths apart. To produce fully sampled images, either the secondary mirror is moved in a so-called jiggle pattern, or the arrays are scanned across the sky in "scan map" mode. For both of these methods, the secondary mirror also chops at a rate of 7.8 Hz to remove most of the sky emission. The jiggle mode is ideal for sources smaller than the field of view of the arrays ($2.3'$), while scan mapping is used for more extended sources. Further technical details of observing with SCUBA on the JCMT are described by Holland et al. (1999).

A sample of 24 compact Lynds clouds was observed in 1997 September using jiggle mode, before scan mapping was fully commissioned (Paper I). Three larger clouds were also scan-mapped at this time as part of the commissioning of this mode (L663, L1165, and L1262). Weather conditions were average and stable (zenith atmospheric opacity at 850 μm, τ_{850} = 0.2−0.7) but not good enough to obtain 450-μm data. A further 15 clouds were scan mapped under extremely good weather conditions (τ_{850} = 0.12) in 1998 July, providing good data at both 850 and 450 μm. Measurements at 450 μm were also made of some of the clouds observed in 1997 during this second observing run. The total survey of 42 clouds covered an area of

~ 0.5 deg^2, or ~ 7 pc^2 for the distances listed in Table 1. Table 3 indicates whether a cloud was observed in jiggle mode or scan mode.

The sky transmission was monitored by performing sky dips throughout each night, and the telescope pointing was checked regularly using nearby bright sources (usually a blazar or a planet). The pointing accuracy was $2''$–$3''$. The focus and alignment of the secondary mirror were also checked two or three times every night. The absolute calibration is obtained from observations of Mars and Uranus, observed using the same mode and chop throw as the observations of the dark clouds.

The chop throw for the jiggle maps was $150''$, with the chop direction dependent on the structure of the cloud. To remove slowly varying background emission, instrumental offsets in SCUBA, and telescope asymmetries, the telescope is also nodded every 16 s to place the source in the opposite beam.

When mapping extended sources in scan-map mode, smaller chop throws must be used to avoid significant degredation of the beam efficiency at the edges of the arrays. In addition, the telescope is not nodded, so that instrumental and other offsets have to be established during the data reduction using baselining algorithms. The resulting maps are images of the sky convolved with a dual beam function, which is the single telescope beam convolved with positive and negative delta functions separated by the chop throw (the chop function). The chop function must be deconvolved from the image to obtain a representation of the sky. Conceptually, this deconvolution is equivalent to a division of the Fourier transform (FT) of the image by the FT of the chop function. The FT of the chop function, however, is a sine function, and clearly problems will arise at spatial frequencies close to nulls in the sine function, where the noise will be greatly amplified by the division.

There are two ways of solving the problem of noise amplification near nulls in the sine function, and both have been used here. The conventional observing method is to scan the telescope in the same direction as the chop throw (usually azimuth). The resulting dual-beam map can be restored with the Emerson-Klein-Haslam (EKH) algorithm (Emerson, Klein, & Haslam 1979). The deconvolution of the chop function is essentially carried out by dividing the FT of the map with a weighted FT of the chop function, where the weighting excludes spatial frequencies which have been attenuated to less than 0.5 of their original amplitude. The scan maps obtained during commissioning of this mode were observed in this way.

The other method is the "Emerson2" technique (Emerson 1995; Jenness, Lightfoot, & Holland 1998), used during the 1998 July observations. Here six maps are made, three of which are chopped in right ascension, and three of which are chopped in declination. Chop throws of $20''$, $30''$, and $65''$ were used for each map, and the resulting spatial frequency coverage at 850 and 450 μm is shown in Figure 1. With the exception of the zero spatial frequency, these chop throws ensure that the nulls of the FT of each do not coincide, up to the spatial frequency limit of the telescope beam. The disadvantages of not chopping in the azimuth direction (which gives the best subtraction of sky emission and ground spillover) is outweighed by the improved signal-to-noise ratio because of the more efficient deconvolution of the chop function (Jenness et al. 1998).

The data were reduced using the SCUBA User Reduction Facility (SURF; Jenness & Lightfoot 1998). Data from noisy or bad bolometers have been removed. Details of the reduction of the jiggle maps are given by Visser (2000) and Paper I. For the scan maps, a baseline must be removed for each scan and for each bolometer. Various methods for baseline removal are provided in SURF. Some work better than others for a given map, but none is entirely satisfactory, and baseline removal is still an unsolved problem. The chop function is then deconvolved from the data, adjoining maps are mosaicked together and are interpolated from the coordinates of the SCUBA arrays to equatorial coordinates. This interpolation can result in a slight degradation of the resolution, compared with the diffraction beams given above, for both jiggle maps and scan maps. The effective resolution at 850 μm is $\sim 15''$.

The incomplete spatial frequency coverage for scan maps (Fig. 1) results in the low spatial frequencies (corresponding to large-scale structure in the image) being measured with low sensitivity, and the zero spatial frequency (i.e., the total power in the map) not being measured at all. The deconvolution of the chop function is therefore similar in many respects to the deconvolution of the dirty beam from an image made by an interferometer, where an attempt is made to extrapolate the measured visibility function to zero spatial frequency while maintaining consistency with the measured data. In the Emerson2 algorithm as implemented in SURF, the effect is to amplify the noise on low spatial frequencies, so that the final images have the equivalent of "$1/f$" noise in the image plane: spatial scales corresponding to a few chop throws or more are measured with low sensitivity and thus have high noise values, whereas structures on scales between the maximum chop throw and the beam size are measured with dynamic ranges limited only by the thermal noise.

4. Results of the submillimeter continuum imaging

4.1. Cloud structure

The 24 compact Lynds clouds observed using SCUBA in jiggle mode have been presented in Paper I and will not be reproduced here. The 15 clouds detected in scan map mode are shown in Figures 2–16. Contour plots of the 850-μm or 450-μm continuum emission are overlaid on optical images from the STScI Digitized Sky Survey, with contour levels indicated in the figure captions. All the images have been smoothed with a 20$''$ Gaussian (FWHM), apart from those of L158 and L1172 (Figs. 4 and 13), for which a 25$''$ Gaussian was used. This smoothing improves the signal-to-noise ratio in the maps and brings out the faint, extended structure. The smoothing also suppresses high spatial frequency noise introduced by the data reduction process. The area of each cloud surveyed is outlined by a dashed line. Eight clouds from the total of 42 were not detected, five in jiggle mode and three in scan map mode. Further details of these nondetections, including the areas covered by the SCUBA maps of these clouds, are given by Visser (2000). The positions of sources from the *IRAS* PSC are indicated by triangles in each image.

The optical shapes of the clouds in this sample are varied. The clouds L57, L543, L663, and L675 are round and globule-like. The clouds L860, L951, and L1103 appear to have been swept up by a shock or wind and are cometary-like. The structure of L673, on the other hand, is very filamentary. The submillimeter continuum emission also encompasses a wide range of structures. Of the clouds that were detected, some exhibit purely diffuse, extended emission, some contain compact submillimeter sources, and others, such as L63, L694, and L944, have a combination of both. The extended submillimeter emission from L31 and L953 correlates very well with extinction in the optical images.

The extended submillimeter emission from a few clouds does not correlate well with the dust extinction: see, for instance, L162, and the southern part of L673. In the case of L673, this might be caused by poor atmospheric conditions during observation of the southern part. This would increase the noise level towards the south and may also explain why 450-μm emission is only detected towards the northern parts of the cloud. The lowest contour levels in the south may therefore trace correlated noise and is not very reliable. L162 was also observed under less than optimum weather conditions. In general, scan maps can sometimes exhibit not only suspicious extended positive features, but also negative features — artifacts introduced by the deconvolution process and the lack of information at low spatial frequencies. Several techniques have been used in the literature to solve this problem, such as fitting two-dimensional polynomials or surfaces to background emission in the image plane (e.g., Johnstone & Bally 1999; Bianchi et al. 2000). Such methods are, however, ad hoc, and no such subtraction has been performed on the images presented in Figures 2–16. Unsatisfactory as this may be, uncertainty in the structure of extended features in these images will not affect the identification of compact objects such as protostars and starless cores.

4.2. General properties of the clouds

The peak flux densities in the unsmoothed maps are listed in Table 3 for both observed wavelengths. The peak position in the 850-μm map of a cloud does not necessarily coincide with the peak position in the 450-μm image (see, e.g., L63 in Fig. 3). For those scan maps exhibiting negative features the peak fluxes have been measured from a local zero level, determined from cuts through the peak of the emission. This increased the peak flux densities of 10 sources by $\sim 10\%$. The total systematic error in the 450 and 850-μm peak flux densities is about 50% and 20% respectively, and is due to negative features and fluctuations in the optical depth of the atmosphere. Also presented in Table 3 are the statistical uncertainties and integrated flux densities for extended emission. The typical noise level in a 850-μm map is 25 mJy beam^{-1}. The noise levels on the 850-μm EKH maps of L663, L1165, and L1262 are considerably higher, however, because of the poor weather conditions. The integrated flux densities were obtained by summing the flux density within a box around the extended emission of the cloud. The box sizes varied depending on the size of the clouds, but the boxes always covered the extended emission down to the 1σ detection limit, staying clear of the noisy edges of the maps. No correction has been made for the (potentially spurious) negative or positive features in the scan maps when measuring the integrated flux densities.

The 850-μm peak flux densities have been used to calculate masses, column densities, space densities, and extinction, A_V, and are presented in Table 3. Assuming low optical depth at 850 μm the total mass (gas plus dust) traced by the submillimeter dust emission is found from $M = D^2 F_\nu / B_\nu(T)\kappa_\nu$, where D is the distance to the source, F_ν is the flux density at frequency ν, $B_\nu(T)$ is the Planck function for dust temperature T, and κ_ν is the dust opacity per unit mass of gas plus dust. For $\kappa_{850\mu\mathrm{m}} = 0.0012$ m^2 kg^{-1}, and a temperature $T = 12$ K, this gives $(M/M_\odot) = 1.9 \times 10^{-8}(D/\mathrm{pc})^2[F_{850\mu\mathrm{m}}/(\mathrm{mJy\ beam}^{-1})]$. The peak masses obtained in this way range from 0.04 $M_\odot$ to 4.07 $M_\odot$. The column density has been calculated using $N(\mathrm{H_2}) = F_\nu / B_\nu(T)\kappa_\nu m_{\mathrm{H_2}}\mu\Omega_b$, where $m_{\mathrm{H_2}}$ is the mass of an H_2 molecule, μ is the mean molecular weight of the particles, assumed to be 1.36, and Ω_b is the solid angle of the beam. For the same values of $\kappa_{850\mu\mathrm{m}}$ and T used above and $\Omega_b = 15''$, this reduces to $[N(\mathrm{H_2})/\mathrm{m^{-2}}] = 1.33 \times 10^{24}[F_{850\mu\mathrm{m}}/(\mathrm{mJy\ beam^{-1}})]$. An estimate of the mean space density is obtained by assuming the depth of the cloud is similar to the beamsize at the distance of the cloud. The mean peak column density is $3.9 \times 10^{26}\ \mathrm{m^{-2}}$, and the mean peak density is $7.6 \times 10^{11}\ \mathrm{m^{-3}}$, but the values for individual clouds cover a broad range. The peak extinction is calculated using $(A_V/\mathrm{mag}) = N(\mathrm{H_2})/(0.95 \times 10^{25}\ \mathrm{m^{-2}})$ (Bohlin, Savage, & Drake 1978), and for the detected clouds all have $A_V \geq 8$ mag, agreeing well with that measured for dark clouds using isotopomers of CO (Myers, Linke, & Benson 1983). The total gas mass and mean column densities are also presented in Table 3, calculated using the integrated flux densities. The total mass observed in the survey is $\sim 400\ M_\odot$, with the most mass ($\sim 90\ M_\odot$) associated with L673. The mean cloud column density varies between ~ 1 and $10 \times 10^{25}\ \mathrm{m^{-2}}$ with three exceptions: L663, L1165, and L1262. These three clouds were those observed with the EKH technique, and the dynamic range on these maps is too small to be able to detect the lower column densities.

It is clear that the above calculations of mass, column, and space densities depend on the assumptions made about the dust opacity, dust temperature, and distance of the cloud. The dust opacity used is that of Hildebrand (1983) and is probably uncertain by a factor of 3 or so (Henning, Michel, & Stognienko 1995). The assumed dust temperature of 12 K is typical for quiescent, dark, molecular clouds (Myers et al. 1983) but is likely to be an underestimate for those clouds containing young stellar objects. Radiation from protostars heat the surrounding material out to $\sim 10^4$ AU (Chandler & Richer 2000), and protostellar outflows can also heat the cloud through shocks. However, temperatures in the range 8–20 K will not change the derived cloud masses by more than a factor of 2. Uncertainties in the cloud distances potentially have a stronger influence on the cloud mass. The numbers presented in Table 3 should therefore be regarded just as indicative of general cloud conditions.

5. A catalog of compact dust cores

The submillimeter images of the 42 Lynds clouds presented in § 4.1 and Paper I show many compact objects, possibly pre-protostellar or protostellar in nature. A compact object not containing a protostar is not necessarily pre-protostellar, however. A dense core must be gravitationally bound before it can collapse and form a star, and it is not possible to determine whether a clump is gravitationally bound from dust emission alone. The term "starless core" is therefore used here to denote a compact source not associated with an outflow.

Various definitions of a "core" can also be found in the literature. Myers et al. (1983) were the first to study cores in dark molecular clouds systematically and defined a core as a small (0.1 pc), dense ($3 \times 10^{10}\ \mathrm{m^{-3}}$), and cold (10 K) condensation which is close to stable equilibrium and *may* evolve into a low-mass star. Williams, Blitz, & McKee (2000) define a core as a region in which a single star (or multiple system such as a binary) forms and which is gravitationally bound. Here we use the term core to refer to the compact submillimeter objects in the SCUBA survey, which are not necessarily gravitationally bound.

5.1. Identification of the cores

Compact submillimeter (SMM) objects in the Lynds clouds have been identified by spatially filtering the SCUBA images. Each map was smoothed with a $2'$ Gaussian, and the smoothed map was then subtracted from the original image. This removed all large cloud structures, as well as the unreliable positive and negative features resulting from the beam deconvolution of the scan maps. The remaining image contains only compact structures, and all structures at a level $\geq 3\sigma$ were identified as cores. Although this method is somewhat subjective, it does select in a quantitative way all the features seen by eye, and all known protostars and pre-protostellar cores. Ideally, one would like to use a fixed physical scale (such as a limiting A_V) to select the dense cores. However, this fixed value would be dominated by the noisiest map.

Forty SMM cores were identified in the manner described above, and are listed in Table 4. The positions of the cores have been obtained from Gaussian fits to the emission and so do not necessarily coincide exactly with the emission peak. Four cores were rejected from the list (in L31, L55, and two in L917), since they appear near the edge of the map where spiky negative and positive features can occur, a known artifact resulting from the regridding algorithm. L158−SMM2 is suspiciously spiky too, but since it is not near the edge of the map it is included in the list.

There are 10 cores that lie within $12''$ of sources in the *IRAS* PSC and so can be directly associated with those sources. These associations are listed in Table 4. All 10 cores are known protostars. Both L673−SMM1 and L1709−SMM5 lie within $40''$ of an *IRAS* source (19180+1116 and 16285−2356, respectively) and are possible associations. In order to verify these possible assocations, HIRES images of the *IRAS* data for L673 and L1709 were obtained from IPAC[2]. Figures 17 and 18 demonstrate that IRAS 19180+1116 can confidently be associated with L673−SMM1, and IRAS 16285−2356 with L1709−SMM5.

Figure 19 shows 850 μm emission from all the cores in the sample on the same angular scale, with the central positions from Table 4 marked as stars. All associated *IRAS* sources are very near the core positions, apart from IRAS 19180+1116 and 16285−2356. Some of the cores are very compact and round (see, e.g., L260−SMM1, L673−SMM1, and L1262−SMM1), while others are more extended (e.g., L63−SMM1, L158−SMM1, and L673−SMM8). It has been suggested that emission from T Tauri stars and Class I sources is more centrally condensed than emission from Class 0 sources (André & Montmerle 1994). Certainly, the only T Tauri star detected, L162−SMM1, is very compact, as expected. L63−SMM1, a starless core, appears extended, and the known protostars vary from compact (L483−SMM1) to very compact (L1709−SMM1). Figures 20 and 21 illustrate the locations of the submillimeter cores in L673 and L1709, the two clouds containing multiple sources.

---

[2]The infrared Processing and Analysis Center (IPAC) is funded by NASA as part of the *Infrared Astronomical Satellite (IRAS)* extended mission under contract to the Jet Propulsion Laboratory.

5.2. Completeness

The detection limit in terms of mass is different for each cloud, owing to varying noise levels and distances. In order to establish that we have complete (or at least representative) samples of starless cores, Class 0, and Class I sources down to a certain mass limit, we must consider each of these effects. Starless cores and Class 0 sources are easier to detect than Class I sources at submillimeter wavelengths. Class 0 sources (for which the envelope mass, $M_{\rm env}$, is greater than the mass of the forming protostar, M_*) have more material in their envelopes than Class I sources (for which $M_{\rm env} < M_*$), and starless, pre-protostellar objects still have *all* their material in an "envelope", since they have not yet formed a hydrostatic protostellar core. Our main problem is, therefore, potentially missing Class I sources associated with the observed Lynds clouds.

In § 9, we compare the detection rates of Class 0 and Class I sources in our sample with those previously observed for ρ Ophiuchus by André & Montmerle (1994), for which the detected ratio of Class 0 sources to Class I was 1:10. In order for such a comparison to be meaningful, it is important to establish whether our samples of Class I protostars meet the same completeness criteria. André & Montmerle found that, for Class I sources in ρ Ophiuchus, $M_{\rm env}$ ranges from $\sim 0.015\ M_\odot$ to $\sim 0.15\ M_\odot$, with a median value of $\sim 0.06\ M_\odot$, assuming a dust temperature of 30 K, and $\kappa_{1.3\rm mm} = 0.001$ m^2 kg^{-1}. The detection mass limit for the Lynds clouds mapped using SCUBA can be calculated using these same parameters, adopting a 3σ flux detection limit, the distances given in Table 1, and scaling $\kappa_{1.3\rm mm}$ to a wavelength of 850 μm assuming a frequency dependent dust opacity, $\kappa_\nu \propto \nu^\beta$, with $\beta = 1.5$. The detection limit for most clouds is then $< 0.015\ M_\odot$ in our survey. Only the furthest clouds (L543, L771, L860, L917, L944, L951, L953, L1172, and L1246) and the clouds for which the maps are noisy (L663, L1165, and L1262) have higher mass detection limits, ranging from $\sim 0.02\ M_\odot$ to $\sim 0.09\ M_\odot$. We could, therefore, have missed some Class I sources in these clouds. However, we would still have expected these sources to have been detected by *IRAS*: even for the most distant cloud its 60 μm detection limit of 0.25 Jy is equivalent to $M_{\rm env} \sim 0.003\ M_\odot$.

In total, there are nine *IRAS* sources associated with the clouds mentioned above (Table 2), and five of these sources are known protostars, which we have detected. We do, therefore, need to investigate the nature of the remaining four *IRAS* sources in order to exclude the possibility that these are low-mass Class I protostars, undetected in the SCUBA maps. The *IRAS* colors of 22051+5849 in L1165 do not correspond to those of a protostar, and this is certainly not a Class I source. Two *IRAS* sources not detected as submillimeter cores, 19343+0727 in L663 and 19186+2325 in L771, do have the colors consistent with being protostellar, but these sources can be identified with bright, optically visible stars. The remaining undetected *IRAS* source is 21186+4320, a source with an entry in the PSC at only 100 μm. A HIRES 60 μm image of this cloud showed far-infrared emission displaced from the PSC position, and the 60 μm peak in the HIRES map was not covered by the SCUBA image. None of the undetected *IRAS* sources is therefore a Class I source, and our sample of submillimeter cores should be complete for Class I sources down to $M_{\rm env} = 0.015\ M_\odot$.

6. A ^{12}CO J=2–1 survey for outflows from the compact cores

6.1. Observations

To determine the nature of the newly identified compact cores a search for outflows was carried out in the J=2–1 transition of ^{12}CO (230.538 GHz) using receiver A2 on the JCMT. Observations were made in 1998 July and by JCMT staff in service mode throughout 1999. Spectra were obtained in a five- or nine-point pattern, with the central spectrum on the dust peak from the SCUBA 850 μm map. The system temperature was typically 440 K and the integration time of each spectrum was 2 minutes, to give an rms level of 0.2 K in a bandwidth of 0.16 MHz (0.2 km s^{-1}).

Table 4 shows which submillimeter cores have been searched for outflows and whether or not high-velocity gas was detected. Ten cores were not observed in ^{12}CO(2–1): L483−SMM1 is a well known protostar, whose outflow has already been extensively studied; L162−SMM1 is a T Tauri star; and L158−SMM2 is the unreliable "spiky" source. The other seven cores were not searched owing to limited observing time but seem extended and are unlikely to contain embedded protostars (Fig. 19). They have therefore been classified as "probably starless" cores since, strictly speaking, their nature is still unidentified. Of the 40 cores identified in § 5, 10 are known protostars, eight of which were already known to drive outflows. The two protostars for which this was not known are L162−SMM1 (a Class II object) and L1246−SMM1 (which does show high-velocity line wings in these new data). Of the 30 remaining cores, 22 were searched for high-velocity gas, and the ^{12}CO(2–1) line emission from three of these cores (L673−SMM1, L944−SMM1, and L1709−SMM5) shows high-velocity emission, indicative of an outflow.

Larger maps of the three new outflows and seven of the known eight flows (all but L483−SMM1) were subsequently observed in ^{12}CO(2–1) in 1998 July and throughout 1999 in service mode with receiver A2 on the JCMT. Many of the old maps of the known outflows are incomplete, of poor resolution, or not in ^{12}CO(2–1), and our new observations provide a homogeneous sample. All these maps were made using the on-the-fly mapping mode with a cell size of 5$''$ and an integration time of 5 s per point. The spectra were taken by position-switching to eliminate instrumental and atmospheric effects. Pointing was checked regularly, and the system was calibrated using standard chopper wheel techniques to obtain spectra on the T_A^* scale. The main beam efficiency at this wavelength is 0.66.

6.2. Outflow maps

The large-scale maps of the outflows have been slightly smoothed and are shown in Figures 22–29. Previous observations and results from these new maps are described below.

6.2.1. L260

L260−SMM1 drives a very compact bipolar outflow, which was classed only as an uncertain detection by Bontemps et al. (1996). The outflow has been detected again here. This source has been classified as Class I (Bontemps et al. 1996) and also has been identified optically (Ichikawa & Nishida 1989). Optical identifications are rare for Class I sources, and this fact, together with the detection of only a very compact and weak outflow, suggest that this protostar is either fairly evolved and accreting the last of its material or is being observed close to pole-on (Fig. 22).

6.2.2. L483

The outflow from L483−SMM1 has been extensively studied, so no new map was obtained for this flow. The high-velocity gas exhibits a distinct east-west bipolar structure, with a high degree of symmetry about the *IRAS* source (Parker 1989; Fuller et al. 1995). The low-level, extended emission in the SCUBA images of this source (Fig. 7) reflects the shape of the outflow cavities, as has been observed for the Class 0 protostar L1527 (Chandler & Richer 2000). Indeed, the detection of the outflow from L483−SMM1 in ^{12}CO J=4–3 by Hatchell, Fuller, & Ladd (1999) confirms the presence of heated gas, and the dust emission probably traces this same material.

6.2.3. L663

L663−SMM1 (B335) drives an outflow very similar in structure to that of L483−SMM1 and has also been studied extensively (e.g., Cabrit, Goldsmith, & Snell 1988; Moriarty-Schieven & Snell 1989). The map presented here (Fig. 23) is of limited extent and does not cover the entire outflow but is included for completeness.

6.2.4. L673

The full extent of high-velocity gas in L673 mapped by Armstrong & Winnewisser (1989) in ^{12}CO(1–0) emission is $12'$. The resolution of their map was poor (half-power beamwidth of $3.9'$), however, and it is not clear from their data whether IRAS 19180+1114 or 19180+1116 drives the outflow. Anglada et al. (1997) argue that it is more likely for IRAS 19180+1114 to be the origin of the flow, but our new map (Fig. 24) suggests that both L673−SMM1 (associated with IRAS 19180+1116) and L673−SMM2 (IRAS 19180+1114) have outflows. At least, it is clear that both sources have blueshifted outflow, but the structure of the redshifted gas is more complicated. The situation near the southern cores in L673 is even more confused. A small map ($120'' \times 80''$) was made to cover L673−SMM3 and L673−SMM5, and some high-velocity gas was detected (the ^{12}CO line is 6.5 km s^{-1} wide), so it is possible that one of these two cores is a protostar. The emission from L673−SMM3 is more centrally condensed than L673−SMM5

(Fig. 20) and L673−SMM3 has therefore been classified as a protostar candidate, and L673−SMM5 as a starless core, but more observations are needed to confirm this. Both L673−SMM6 and L673−SMM8 also show some red-shifted high velocity gas, but this is difficult to interpret from the limited ^{12}CO data available. Both cores have therefore been classified as starless.

6.2.5. L944

This protostar is newly detected by this survey, with both the continuum emission and outflow previously unknown. Its outflow is presented in Paper I.

6.2.6. L1165

The bipolar outflow of L1165−SMM1 was partly observed by Parker (1989) but is now fully covered by the new ^{12}CO map (Fig. 25).

6.2.7. L1172

The outflow emanating from L1172 is very extended and was detected in ^{12}CO(1–0) by Myers et al. (1988). Unfortunately, the ^{12}CO(2–1) map presented here covers only a part of the outflow owing to limited observing time and includes L1172−SMM2 but not L1172−SMM1 (see Fig. 26). It is, however, more likely that L1172−SMM1 drives the outflow, since this submillimeter source is closer to the *IRAS* source. L1172−SMM1 has, therefore, been classified as a protostar, and L1172−SMM2 as starless. The properties of this outflow have not been studied further, owing to the limited map.

6.2.8. L1246

L1246−SMM1 is a previously known protostar (Launhardt et al. 1997), but an outflow had not been detected, despite sensitive searches (Parker et al. 1991). The CO outflow has now been detected and mapped, confirming the protostellar nature of this source, and is presented in Paper I.

6.2.9. L1262

The bipolar outflow from L1262−SMM1 has been observed by Bontemps et al. (1996). The new map made with the JCMT is larger in extent and is shown in Figure 27.

6.2.10. L1709

A blueshifted outflow driven by L1709−SMM1 has been presented by Bontemps et al. (1996). Parker (1989) noted, however, that a redshifted outflow is very likely also present, and this redshifted outflow has now been detected (Fig. 28). A new outflow emanating from L1709−SMM5 has also been mapped (Fig. 29). Spectra obtained in a five-point pattern centered on L1709−SMM3 showed some redshifted, high-velocity gas, but this is probably due to the outflow emanating from L1709−SMM1, and L1709−SMM3 has been classified as starless.

6.3. Outflow dynamics

The dynamical properties of the observed outflows are given in Table 5. The mass of high-velocity molecular gas in the outflows has been calculated assuming low optical depth and local thermodynamic equilibrium with an excitation temperature of $T_{\rm ex} = 20$ K. The abundance of ^{12}CO relative to H_2 is assumed to be 5×10^{-5}, and the distances used in the calculations are those in Table 1. The kinetic energy in the flow, $\Sigma MV^2/2$, has been calculated for velocity intervals of 0.5 km s^{-1} or 1.0 km s^{-1} and summed. For example, the energy in the L1262 outflow is summed between 6 and 10.5 km s^{-1} for the redshifted gas and between -3 and 2 km s^{-1} for the blueshifted gas. The velocity boundaries for each outflow were established by comparison with an "ambient" spectrum obtained away from the outflow, using the same criteria as those of Bontemps et al. (1996): the high-velocity bound of the blueshifted wing (and low-velocity bound of the redshifted wing) was chosen to be the velocity at which the ambient spectrum had $T_A^* = T_{\rm peak}/10$ on the blue side (red side); the low-velocity bound of the blueshifted wing (and high-velocity bound of the redshifted wing) corresponds to the velocity at which emission is no longer positively detected above the noise. The extent of the outflow is the distance from the core to the edge of the redshifted outflow plus the core to the edge of the blueshifted outflow. The outflow in L663 has not been completely mapped, and the extent measured is therefore a lower limit. The velocity width is the total width of the outflow at the 1σ noise level. The dynamical age, τ_d, is the outflow extent divided by the velocity width and is an indication of the lifetime of the outflow. No correction has been made for flow inclination in calculating the above quantities.

The momentum flux (or force) of an outflow is the ratio of the flow momentum to the dynamical age. We have applied a correction factor of 10 in calculating the values of the momentum flux displayed in Table 5 to account for a combination of the optical depth of the CO emission and a mean inclination angle of the flow, thereby enabling a direct comparison with the momentum fluxes presented by Bontemps et al. (1996). Bontemps et al. argue that, if outflows are momentum driven and momentum is conserved along the flow direction, full maps of an outflow are not needed in order to obtain an estimate of the momentum flux. In the case of L663−SMM1 (B335) we have investigated this by comparison with values from the literature. Based on a map even more limited than that shown in Figure 23, Bontemps et al. derive a momentum flux (corrected using the above factor of 10 for line opacity and flow inclination) for the L663 outflow of 1.2×10^{-5} $M_\odot$ km s^{-1} yr^{-1}. These authors do not specify the assumed ^{12}CO to H_2 abundance used in their calculations, although much of their analysis is compared directly with the work of Cabrit & Bertout (1992), who use a value of 1×10^{-4}, a factor of 2 higher than that assumed here. Converting the Bontemps et al. value for the momentum flux to an abundance of 5×10^{-5} therefore gives 2.4×10^{-5} $M_{\odot}$ km s^{-1} yr^{-1}. Cabrit et al. (1988) mapped the entire flow, and using a ^{12}CO to H_2 abundance of 1.8×10^{-4} obtain a momentum flux of 2.4×10^{-5} $M_{\odot}$ km s^{-1} yr^{-1}, including measured corrections for optical depth and flow inclination. Converting this to the same abundance used here gives 8.6×10^{-5} $M_{\odot}$ km s^{-1} yr^{-1}. Our value for the momentum flux of 4.7×10^{-5} $M_{\odot}$ km s^{-1} yr^{-1} lies in the same range as those previously reported, when the different abundances assumed are taken into account. Thus, to within a factor of a few, the estimates of the outflow momentum flux using the Bontemps et al. assumptions seem reasonable and can be used for qualitative comparisons within the sample, since they are calculated for all sources in a consistent manner.

Most of the outflows are clearly bipolar. The outflows emanating from L260−SMM1 and L1709−SMM5 have their red- and blueshifted lobes overlapping to a large degree, and we may be observing these flows close to pole-on. The outflows in L673 are the most complex. The two submillimeter cores clearly drive blueshifted outflows, but it is less obvious which source drives the redshifted gas. The outflow properties of both L673−SMM1 and L673−SMM2 in Table 5 are therefore based only on the blueshifted gas. The redshifted outflow is very massive (0.07 $M_{\odot}$) and energetic (2.2×10^{36} J) compared with the other outflows in the sample and may be a combination of flows associated with both cores.

7. Classification of the protostars

A statistical analysis of source properties and relative lifetimes requires that all the protostars in our sample be classified according to some scheme approximating age or evolutionary status. Several such classifications have been used in the past, from the rather coarse division according to the near- to mid-infrared SED to the more continuous bolometric temperature ($T_{\rm bol}$). Other source properties have also been found to correlate with either the SED classification or $T_{\rm bol}$, the subsequent interpretation of which can be somewhat model-dependent. Here, we place the protostars observed in our sample into these classification schemes and compare the results with those reported in the literature.

7.1. Spectral energy distributions

The flux densities of the protostars at 450 and 850 μm in a 50″ aperture have been measured after having subtracted background emission and are presented in Table 6. For those sources with previously published submillimeter flux densities (L483−SMM1, L663−SMM1, L1172−SMM1, L1246−SMM1, and L1262−SMM1; see Launhardt et al. 1997; Huard, Sandell, & Weintraub 1999; Shirley et al. 2000), our measurements are in good agreement with those earlier results. Our 450 and 850 μm data are also plotted in Figure 30, along with the far-infrared *IRAS* fluxes from Table 2. The protostar L944−SMM1 is not associated with an *IRAS* source from the PSC, but its far-infrared flux densities were obtained from HIRES data, as described in Paper I. Far-infrared flux densities for the protostars in L673 and L1709, where inspection of Table 2 indicates considerable confusion in the PSC, were also obtained from HIRES images (Figs. 17 and 18) for all *IRAS* bands except 100 μm, for which the resolution is insufficient to separate emission from the multiple sources. Upper limits only are therefore given for 100 μm flux densities. At 60, 25, and 12 μm, the emission was integrated in a box around the protostar after subtraction of a background level (a circular aperture does not work here because of the elliptical *IRAS* beam). The HIRES flux densities are listed in Table 7; the absolute uncertainty in these values is $\sim 30\%$.

The SEDs have been fitted with a single-temperature gray-body spectrum, $F_\nu \propto \nu^\beta B_\nu(T_{\rm dust})$. The dust emission is assumed to be optically thin, and β is fixed at 1.5. The fitted values of the dust temperature, $T_{\rm dust}$, are given in Table 6, and spectra are plotted in Figure 30. Where available, the gray-body spectrum is fitted to 850, 450, and 100 μm data. For the protostars with no 450 μm flux density measurement, only the 850 and 100 μm flux densities are used (i.e., for L162−SMM1, L633−SMM1, L1165−SMM1, and L1262−SMM1). For the four protostars with 100 μm upper limits, the 850, 450, and 60 μm flux densities are used (i.e., L673−SMM1, L673−SMM2, L1709−SMM1 and L1709−SMM5). All fits have $\chi^2_\nu < 1$ apart from L1709−SMM5, for which $\chi^2_\nu = 1.3$.

In order to classify the protostars according to the scheme proposed by Lada & Wilking (1984) based on the near- to mid-infrared spectral index and extended to sources not detected in the infrared by André et al. (1993), infrared measurements are needed. L162−SMM1 is an optically-identified T Tauri star (Ichikawa & Nishida 1989) and is classified as Class II by André & Montmerle (1994). The protostars detected in the near-infrared are L260−SMM1 (Myers et al. 1987), L1165−SMM1 (Tapia et al. 1997), and L1709−SMM1 (Myers et al. 1987), and so are Class I protostars. The Class 0 protostars not detected in the near-infrared are L483−SMM1 (Fuller et al. 1995) and L663−SMM1 (Hodapp 1998). L1246−SMM1 and L1262−SMM1 have been classified as Class 0 sources by Launhardt et al. (1997) based on unpublished near-infrared photometry. The remaining five protostars have to be classified without near-infrared measurments.

7.1.1. *Ratio of* $L_{\rm bol}/L_{\rm submm}$

A method proposed for classifying protostars by André et al. (1993) that does not depend on near- and mid-infrared detections is to evaluate the ratio $L_{\rm bol}/L_{\rm submm}$, which for a constant mass accretion rate should be approximately proportional to $M_*/M_{\rm env}$. The ratio $L_{\rm bol}/L_{\rm submm}$ will increase with age, as material from the envelope is accreted onto the protostar. André et al. classify protostars as Class 0 when $L_{\rm bol}/L_{\rm submm} < 200$, where $L_{\rm bol}$ is measured from 1 to 1300 μm, and $L_{\rm submm}$ is the submillimeter luminosity from 350 to 1300 μm. Unfortunately, $L_{\rm bol}$ cannot be determined without near-infrared measurements, and the best we can do here is to calculate the luminosity from 12 to 1300 μm. This will underestimate $L_{\rm bol}$, particularly for the older sources. Lower limits to $L_{\rm bol}$ have therefore been calculated by integrating under the gray-body fit from 1300 to 150 μm and by regarding the *IRAS* PSC or HIRES upper limits as real detections. This latter assumption may tend to overestimate $L_{\rm bol}$, and Figure 30 shows it will affect mainly those protostars not detected by *IRAS* at 12 μm. For both L663−SMM1 and L944−SMM1, which are not detected at either

12 or 25 μm, the bolometric luminosity has been calculated by integrating under the gray-body fit only. Estimates of $L_{\rm bol}$, $L_{\rm submm}$, and $L_{\rm bol}/L_{\rm submm}$ are listed in Table 6. Applying the criterion that a protostar is a Class 0 source when $L_{\rm bol}/L_{\rm submm} < 200$ results in only one Class I source in this sample, suggesting that a different limit should be used for a sample that does not include near-infrared emission in determining $L_{\rm bol}$. Indeed, a limit of $\sim$ 50 is needed to reproduce most of the classifications of those protostars with previous measurements or good upper limits in the near- and mid-infrared. The only source which then does not match its previous classification is L483−SMM1, which has recently been described as a transition Class 0/Class I object by Tafalla et al. (2000) based on a study of the emission from various molecular species.

7.1.2. Bolometric temperature

A more continuous indicator of age, the bolometric temperature ($T_{\rm bol}$), was introduced by Myers & Ladd (1993). $T_{\rm bol}$ is the temperature of a blackbody having the same mean frequency as the observed continuum spectrum and is a measure of circumstellar obscuration. Chen et al. (1995) quantify the Class 0/Class I boundary as $T_{\rm bol} = 70$ K and Class I/Class II as $T_{\rm bol} = 650$ K. Table 6 lists values of $T_{\rm bol}$ derived from the SEDs in Figure 30 in a manner similar to the measurement of $L_{\rm bol}$ described above. Again, the lack of near- and mid-infrared data for these sources will tend to lower the derived $T_{\rm bol}$. Nevertheless, the values in Table 6 should be a good indicator of evolutionary state, albeit with different class boundaries from those obtained by Chen et al. L162−SMM1 has a $T_{\rm bol}$ considerably lower than the 650 K limit assigned by Chen et al., but this source is also likely to be the most seriously affected by the lack of near-infrared data included in its SED. A Class 0/Class I boundary at $T_{\rm bol} = 65$ K gives reasonably good agreement with previous classifications for the other protostars. The class implied for L1709−SMM5 obtained from its $T_{\rm bol}$ is not consistent with that implied by its $L_{\rm bol}/L_{\rm submm}$, and this source may be a transition object similar to L483−SMM1.

7.2. Envelope masses

The mass of circumstellar material associated with each protostar has been estimated from its 850 μm flux density and the dust temperature derived from fitting its SED and is also given in Table 6. A dust opacity $\kappa_{850\mu{\rm m}} = 0.002$ m^2 kg^{-1} has been assumed, consistent with the 1.3 mm dust opacity recommended by Ossenkopf & Henning (1994) for very dense regions, for $\beta = 1.5$. The envelope masses of the protostars obtained in this way range from 0.01 to 2.15 $M_\odot$, and agree well with masses derived by other authors for previously known sources (Bontemps et al. 1996; Launhardt et al. 1997; André, Ward-Thompson, & Barsony 2000).

7.2.1. Ratio of $M_{\rm env}/L_{\rm bol}$

Under the assumption that Class 0 and Class I protostars derive their luminosity primarily from accretion such that $L_{\rm bol} = GM_*\dot{M}/R_*$, and that the accretion rate, $\dot{M}$, and stellar radius, R_*, are constant, the ratio $M_{\rm env}/L_{\rm bol}$ is proportional to $M_{\rm env}/M_*$. If the Class 0/Class I division is set at $M_{\rm env}/M_* = 1$ (such that Class 0 sources have $M_{\rm env}/M_* > 1$), then $\dot{M} = 10^{-6} M_\odot$ yr^{-1} and $R_* = 3R_\odot$ results in $M_{\rm env}/L_{\rm bol} > 0.1 M_\odot/L_\odot$ for Class 0 sources (André & Montmerle 1994). This criterion for classification identifies those same objects as Class 0 sources as does the $L_{\rm bol}/L_{\rm submm} > 50$ criterion above (§ 7.1.1; see also Table 6).

7.3. Outflow properties

A correlation between outflow momentum flux, $F_{\rm CO}$, with envelope mass was found by Bontemps et al. (1996) and has been confirmed for other source samples (e.g., Henning & Launhardt 1998). Class 0 sources drive more powerful and better-collimated outflows than Class I protostars. Figure 31 plots $F_{\rm CO}$ versus $M_{\rm env}$ for the 10 protostars for which we have outflow data (Figs. 22–29). The outflow momentum flux for both L673−SMM1 and L673−SMM2 are lower limits owing to the confusion concerning the red outflow. The dashed line plotted is the best linear fit between $\log F_{\rm CO}$ and $\log M_{\rm env}$ found by Bontemps et al. (1996). It is clear that the momentum fluxes of outflows in our sample agree very well with those observed by Bontemps et al., with only two sources lying at some distance from the relationship found by those authors. These are L1246−SMM1 (the Class 0 source, to the right of the dashed line in Fig. 31), and L1709−SMM5 (the Class I source to the left of the dashed line). The displacement of L1246−SMM1 might be explained by a wrongly-assigned distance. It is listed in Table 1 as having $D = 730$ pc, and as such is the most distant in this sample. If this source were actually closer, its position in Figure 31 would shift to the left and down, since $M_{\rm env} \propto D^2$ and $F_{\rm CO} \propto D$. The overlapping red- and blueshifted lobes of the L1709−SMM5 outflow was suggested above (§ 6.3) to indicate we may be observing this source pole-on. Were this the case, the correction factor applied to $F_{\rm CO}$ that accounts for a mean inclination angle and CO line optical depth may be severely overestimated and could explain the location of this source in Figure 31.

Bontemps et al. (1996) also find that outflows from Class 0 protostars are more efficient than those from Class I protostars, when $F_{\rm CO}$ is compared with the maximum momentum flux available in stellar photons, $L_{\rm bol}/c$. The outflow efficiency, given by the ratio $F_{\rm CO}c/L_{\rm bol}$, is listed in Table 6 for the 10 outflow sources mapped, and this trend is clearly evident: the Class 0 sources typically have $F_{\rm CO}c/L_{\rm bol} \gtrsim 300$. Table 6 also illustrates the nature of L1709−SMM5 as an object in transition between Class 0 and Class I. L1246−SMM1 again stands out as having an outflow considerably weaker than other Class 0 sources. The outflow efficiency scales as $1/D$, so an overestimated distance might again help bring this source into line with the others in this sample. The distance of L1246 has been estimated by associating it with Cep OB3 (Paper I). If it were close enough to raise its outflow efficiency by the factor of 4 or 5 needed to bring it in line with to the Bontemps et al. correlation, it would have to be rather isolated.

7.4. Sizes

The emission from the Class 0 sources is extended, and some objects, such as L483−SMM1, clearly exhibit structure related to the outflow. All the sources identified as Class I protostars in Table 6 are unresolved apart from L1709−SMM5. L1709−SMM5 stands out among all the cores identified as protostellar in nature as being the most extended, and in many respects resembles the starless cores. This raises the possibility that L1709−SMM5 in fact comprises several sources in superposition along the line of sight. Higher resolution observations are needed to confirm this idea.

8. Physical properties of the starless cores

The masses, column densities, and inferred space densities of those cores not containing embedded protostars are listed in Table 8, along with the protostar candidate L673−SMM3. The integrated flux densities at 850 μm have been measured within an aperture after the subtraction of background emission, as described in § 5.1. For some of the more extended cores, such as L260−SMM2, the subtraction of background emission may subtract extended emission from the core itself. However, in most cases, the background subtraction is clearly desirable in order to obtain integrated flux densities representing only the compact submillimeter core. The size of the aperture used was determined from radially averaged intensity profiles, after background subtraction, to include all the observed emission. Table 8 gives the diameter of the aperture used for each core. The masses were calculated assuming $T_{\rm dust} = 12$ K and $\kappa_{850\mu{\rm m}} = 0.001$ m^2 kg^{-1}. The space densities assume that the core has a depth along the line of sight the same as the aperture diameter. The mean mass of the cores is 1.1 $M_\odot$, the mean column density 3.4×10^{25} m^{-2}, and the mean space density 1.0×10^{10} m^{-3}.

The masses of the starless cores are systematically higher than those of the protostellar envelopes by approximately 0.6 $M_\odot$. If the starless cores are indeed the progenitors of the protostars in this sample, we might therefore expect that the starless cores will, in time, produce stars of $\sim$ 0.5–1 $M_\odot$. This result must be taken with some caution, since different dust opacities and dust temperatures have been used for calculating the masses for each population, in such a way that these two factors both serve to increase the apparent mass of the starless cores. However, the assumption that the temperatures in the protostellar envelopes are higher than those in the starless cores is probably a good one, and even if the same dust opacity were used for all sources, the starless cores would still be more massive than the protostellar envelopes.

The 26 starless cores in Table 8 represent the largest sample of these objects for which submillimeter continuum images have been made to date and therefore provide a unique dataset with which to study the properties of these objects. In particular, if the cores are isothermal, the radial intensity profile of the submillimeter emission can be directly inverted to determine the radial density profile in the cores. Analytic and numerical studies show that the mass infall rate during the protostellar phase depends on the radial density profile at the onset of collapse and on the equation of state of the material. Singular models have an $n \propto r^{-2}$ density profile resulting in a constant accretion rate (Shu 1977). Density profiles with a flatter inner region, however, will result in a high mass infall rate initially, possibly corresponding to the Class 0 phase, followed by a phase with a low accretion rate, possibly corresponding to the Class I phase (Foster & Chevalier 1993; Henriksen, André, & Bontemps 1997). The evolution of a protostar will also depend on whether the core from which it is forming has an "edge." The Shu picture has star formation taking place in an essentially infinite reservoir of material, in which case the final mass of the star being formed will be determined by a local process, such as the interaction between its outflow and accretion. If, however, the core has a well-defined edge, the final stellar mass may determined by the structure of the core in the precollapse phase.

The starless cores that have been studied to date in millimeter/submillimeter continuum emission do not appear to show the r^{-2} density profile predicted by the singular isothermal model of Shu (1977). Instead, they have shallow density profiles in their inner regions, in qualitative agreement with models of magnetically supported cloud cores (Ward-Thompson et al. 1994; André, Ward-Thompson, & Motte 1996; Motte, André, & Neri 1998; Ward-Thompson et al. 1999; Shirley et al. 2000). The density profiles of a number of starless cores have also been studied in absorption in the mid-infrared (Bacmann et al. 2000). These also exhibit density profiles that flatten toward the center, and several also have sharp edges. Such profiles need very strong background magnetic fields to be supported, but they are also well fitted by Bonnor-Ebert-type hydrostatic equilibrium models for isothermal, self-gravitating cores confined by external pressure.

Radial intensity profiles for all the starless cores in our sample were obtained from the SCUBA 850-μm images by averaging data points in a $3''$ wide ring at radius r from the core center (Table 4) from $r = 0''$ to $450''$ or the edge of the map. The mean ellipticity of the starless cores is 1.5, and the assumption of circular symmetry should therefore result in a representative intensity profile (see also André et al. 1996), although there is clearly scope for more detailed modeling. Eighteen of the cores have had DC offsets subtracted to obtain sensible zero levels for the background. Emission from nearby cores or protostars were not removed before the profile fitting. A single power-law model for the density distribution did not fit most of the starless cores, so the intensity profiles have been modeled with a density distribution consisting of two power laws. The density is assumed to have the form $n \propto r^{-\gamma}$ from $r = 100$ AU to a radius r_0, beyond which $n \propto r^{-\delta}$. The density at $r < 100$ AU was assumed to be zero to avoid any singularity. An outer cutoff radius r_1 has also been implemented to model the observed edge of the profile. A temperature $T_{\rm dust} = 12$ K has been assumed, and dust opacity $\kappa_{850\mu{\rm m}} = 0.0012$ m^2 kg^{-1}. The resulting intensity profile was calculated from the model by integrating the density distribution along the line of sight, and convolving it with a $15''$ Gaussian to simulate the JCMT beam at 850 μm. The four parameters r_0, r_1, γ, and δ were then adjusted to produce the best fit. The density at r_0, n_0, was normalized to reproduce the observed flux density.

Profiles of all the starless cores were fitted except for L158−SMM2, which is a suspected artifact of the regridding algorithm (§ 5.1), and L1709−SMM4, which is an extended ridge and clearly should not be modeled by a spherically symmetric core (Fig. 19). All the fitted cores apart from L673−SMM6 and L951−SMM2 show a flat inner part in the intensity profile, with a steepening in the radial power-law exponent beyond r_0, out to r_1, where the intensity profile merges into the background. Excluding these two cores, we find mean values of $\gamma = 0.9 \pm 0.3$ and $\delta = 1.9 \pm 0.3$. Figure 32 shows one of the best fits, L694−SMM1, an average fit, L1262−SMM2, and a very poor fit, L673−SMM7. The parameters of these fits are also given in Table 8. For none of our cores is the radial density profile steeper than r^{-3}, as was found for three starless cores by Bacmann et al. (2000). However, the best-fit values of δ are positively correlated with values of r_1 in our fitting, so that a larger value of δ can, to some extent, be compensated for by a larger value of r_1.

Both the results presented here and previous work seem to rule out the singular isothermal spheres developed by Shu and coworkers (but see also the recent, more detailed, modeling of starless cores by Evans et al. 2001) and the logotropic model having $n \propto r^{-1}$ at large radii proposed by McLaughlin & Pudritz (1997), as the pre-collapse density profile of starless cores. Instead, the radial density profiles resemble more closely those expected for pressure-bounded Ebert spheres (e.g., Foster & Chevalier 1993) or for which magnetic pressure is important (e.g., Ciolek & Mouschovias 1994; Basu & Mouschovias 1995).

9. Statistics, timescales, and implications for low-mass star formation

Assuming star formation is a homogeneous process in our sample of dark clouds, and that the starless cores–Class 0 sources–Class I protostars represent an evolutionary sequence, statistical lifetimes of these different stages can be derived from the relative numbers of objects in these different phases. We find a total of seven Class 0 sources, five Class I sources, one candidate protostar, and 26 starless cores. All these cores and protostars are observed in 21 clouds, i.e., in half of the sample of optically dark molecular clouds. Fifty percent of the clouds are therefore quiescent.

9.1. Ratio of Class 0 to Class I sources

One of the most remarkable results of this survey is that the ratio of Class 0 sources to Class I sources is not 1 to 10, as has been observed in previous surveys of the ρ Ophiuchi main cloud (André & Montmerle 1994; Motte et al. 1998), which are also believed to be complete. Furthermore, this result comes in spite of the fact that a significant fraction of the cores in our sample are associated with the ρ Ophiuchi complex. Separating our sample into those clouds that are associated with ρ Ophiuchus and those that are not results in rather small numbers, but the comparison is nevertheless worth investigating. For the Lynds clouds associated with ρ Ophiuchus (see Table 1), we find three Class I protostars, one Class II source, and 10 starless cores, giving a Class 0 to Class I ratio consistent with earlier results. For the non-ρ Ophiuchi clouds we find seven Class 0 sources, two Class I sources, and 17 starless cores. Excluding the clouds in ρ Ophiuchus therefore makes the potential ratio of Class 0 to Class I sources even higher.

We have considered whether the discrepancy between the ratio of Class 0 to Class I sources observed in Lynds dark clouds compared with that observed for ρ Ophiuchus is the result of the completeness limit of our sample ($M_{\rm env} = 0.015\ M_\odot$). If, for example, the Lynds clouds form predominantly lower mass stars than does ρ Ophiuchus, then our mass completeness limit would be insufficient to detect all the Class I sources associated with the Lynds clouds. In order for such an effect to account for the observed discrepancy, approximately 90% of the Class I sources in the Lynds clouds would have to have $M_{\rm env} < 0.015\ M_\odot$. In a recent study of embedded protostars in the low-mass, star-forming region of Taurus, Motte & André (2001) found that in a total of 23 Class I sources only five have $M_{\rm env} < 0.015\ M_\odot$. It therefore seems unlikely that our completeness limit can account for the discrepancy, unless star formation in the Lynds clouds proceeds very differently from star formation in both Taurus and ρ Ophiuchus.

While there are difficulties in the classification of some of our objects (§ 7), we can fairly easily rule out a 1:10 ratio for the full sample, and the statistics are more consistent with a 1:1 ratio. This suggests that the lifetime of a Class 0 source in a Lynds dark cloud is as long as the lifetime of a Class I source, a result that is supported by the dynamical lifetimes of the outflows. The mean dynamical age of the Class 0 outflows presented here is 2.7×10^4 yr, compared with the Class I outflows of 1.8×10^4 yr. Even if the dynamical lifetime of the outflow in L1246 is overestimated due to the uncertainty in its distance, the mean age of the remaining Class 0 outflows is 2.2×10^4 yr, similar to that measured for the Class I sources.

The lifetime of the Class I phase is believed to be reasonably well established owing to complete infrared surveys of the ρ Ophiuchus and Taurus star forming regions (Wilking et al. 1989; Kenyon et al. 1990). If a lifetime of $\sim 2 \times 10^5$ yr is adopted for Class I protostars, the statistical lifetime of Class 0 sources in this sample will be similar. Of course, this assumes that stars form in molecular clouds continuously and in a homogeneous fashion. However, the different ratio of the numbers of Class 0 to Class I sources found here, compared with other surveys, might indicate that stars do not form in such a homogeneous way, demonstrating that the star formation process is highly dependent on the local environment. There are three ways this might work:

1. Class 0 sources may represent a different branch of star formation and may not be precursors of Class I sources. Indeed, Jayawardhana, Hartmann, & Calvet (2001) have suggested that some Class 0 sources may be protostars forming in very high density regions and are, in fact, at the same evolutionary stage as the Class I sources forming in lower density environments. If this were true, however, it would imply that the Lynds dark clouds are of higher density than the cores in ρ Ophiuchus. A comparison of our results with those of Motte et al. (1998) shows the opposite to be the case.

2. If Class 0 sources are precursors to Class I sources, it may be that the environment, with its local initial conditions, determines how long the Class 0 phase lasts. For example, if the Lynds clouds represent a more quiescent environment than the clouds in ρ Ophiuchus, there may be more time for the starless cores in the Lynds clouds to evolve towards a singular isothermal sphere before the onset of collapse. In this case, the collapse might progress with a constant accretion rate, and the Class 0 phase could then last longer in these clouds. In ρ Ophiuchus, the star formation may be triggered before the starless cores reach a singular state, in which case a more dramatic Class 0 phase (higher accretion rates) would precede the Class I phase. However, none of the starless cores detected here has the characteristics of a singular isothermal sphere on small scales.

3. Perhaps a more likely possibility is that star formation is not a steady process. If star formation relies heavily on triggering, the sample of embedded protostars in ρ Ophiuchus may be dominated by an older, more evolved population due to a burst of star formation some $\sim 10^5$ yr ago. Indeed, on large scales, it is thought that star formation in ρ Ophuichus may have been triggered by a supernova in the

Scorpio-Centaurus OB association (de Geus 1992). Motte et al. (1998) conclude that the small-scale structure of the ρ Ophiuchi main cloud is also consistent with the passage of a shock, and that the youth of the protostars over a large region indicate star formation must have been synchronized by an external mechanism.

The previous, short, lifetimes derived for Class 0 protostars in ρ Ophiuchus also had another important implication for accretion during early protostellar evolution. A distinguishing feature of Class 0 protostars is that they are surrounded by a considerably larger reservoir of circumstellar material than Class I protostars (see, e.g., Table 6), and a short time spent in this phase implied a considerably higher accretion rate for Class 0 protostars compared with the Class I phase. If, instead, protostars spend a similar amount of time in the Class 0 and Class I phases, there may be no such initial period of rapid accretion.

9.2. Ratio of starless cores to protostars

There are 26 starless cores compared with a total of 12 or 13 embedded protostars in our sample of Lynds clouds, so the ratio is approximately 2:1. This suggests that the lifetime of a starless core as detected in the SCUBA survey is only twice as long as the lifetime of an embedded protostar. The lifetime of the Class 0 and Class I phase combined is $\sim 4 \times 10^5$ yr, and from this the estimated lifetime of starless cores is $\sim 8 \times 10^5$ yr. This is only 2–3 times the free-fall time for an average core in the sample, $\sim 3 \times 10^5$ yr. Using the power-law density profiles given in Table 8, we have examined whether the thermal pressure of gas at a temperature of 10–12 K is sufficient to provide support against gravitational collapse for the starless cores on scales $r \sim 10^4$ AU. In all cases, a velocity dispersion of ~ 0.1–0.2 km s^{-1} is required, comparable with the isothermal sound speed for gas at 10 K. It therefore seems entirely feasible that the starless cores are in hydrostatic equilibrium and do not need the support of magnetic fields *on these size scales*. The cores are, therefore, on the verge of collapse, and it is unlikely that strong magnetic fields are important for the collapse dynamics of starless cores once they reach densities of $\sim 10^{10}$ m^{-3}. Of course, this does not rule out the possibility that magnetic fields are important for providing support in molecular clouds on larger size scales, nor does it suggest that magnetic fields may not be important dynamically for the *formation* of the starless cores.

9.3. Ratio of quiescent clouds to star-forming clouds

Since all the compact cores are observed in half the sample of dark clouds the other half of the sample are quiescent clouds. The combined duration of the starless core phase and embedded phase is $\sim 1 \times 10^6$ yr and the statistical lifetime of a quiescent Lynds Class 6 cloud is thus also $\sim 1 \times 10^6$ yr. The comparison made here is, however, difficult, since all the clouds have different sizes, and some of the clouds are complexes of smaller clouds (e.g., L673). Nevertheless, these clouds are known to have reasonably long lifetimes and should at least be stable for long enough to form stars. Some T Tauri stars are also still found in this type of cloud, suggesting that the clouds have lifetimes $\gtrsim 10^6$ yr.

10. Summary and conclusions

We have surveyed a sample of optically selected dark clouds for the submillimeter dust emission associated with embedded protostars and starless dense cores. The optical selection criterion is equivalent to a limiting column density ($A_V \gtrsim 10$ mag) and avoids biases relating to the infrared properties of older protostars and other indicators of star formation potential or activity. Furthermore, the clouds are predominantly nearby, giving a sample for which good spatial resolution can be obtained. All clouds were imaged at $\lambda = 850$ μm, with a spatial resolution of $\sim 2,000$–10,000 AU, depending on the distance. A total of 42 dark clouds, covering an area of 0.5 deg^2, are included in the survey.

Compact submillimeter cores have been identified in the clouds, and we have established whether the cores contain embedded protostars through a combination of association with *IRAS* emission and/or the presence of high-velocity CO(2–1) emission from protostellar outflows. The survey is complete for starless cores, and for Class 0 and Class I protostars, to a mass limit of 0.015 $M_\odot$. Half of the clouds, 21 in total, do not contain any compact submillimeter cores and are therefore quiescent as far as star formation activity is concerned. The other half contain a total of seven Class 0 protostars, five Class I protostars, one Class II source, a candidate protostar (L673$-$SMM3), and 26 starless cores. The ratio of Class 0 to Class I protostars found in this survey is therefore close to unity and is not consistent with the previous result found for the ρ Ophiuchi cloud, where a ratio of 1 to 10 has been observed (André & Montmerle 1994; Motte et al. 1998). The ratio of starless cores to cores containing embedded protostars is approximately 2 to 1. The implied lifetimes of the Class 0 and starless core phases are therefore $\sim 2 \times 10^5$ yr and $\sim 8 \times 10^5$ yr, respectively.

The different ratio of Class 0 to Class I protostars detected in our survey compared with previous work suggests star formation is highly dependent on the local environment. Our new results provide several possibilities for the nature of low-mass star formation: (1) Class 0 sources are at the same evolutionary stage as Class I sources, but represent a different branch of star formation, e.g., star formation in high density environments. However, a comparison between our study and that of Motte et al. (1998) suggests the Lynds clouds are actually less dense than those in ρ Ophiuchus. (2) If Class 0 sources are precursors to Class I sources, the local environment may determine the lifetime of the Class 0 phase. For example, if the Lynds clouds are more quiescent than those in ρ Ophiuchus, they may have more time to evolve towards the singular $n \propto r^{-2}$, which predicts a more uniform accretion rate. However, none of the starless cores detected here has the characteristics of a singular isothermal sphere. (3) Star formation is not steady, and relies heavily on triggering. The ratio of Class 0 to Class I protostars in ρ Ophiuchus can then be explained by being dominated by an older, more evolved population caused by a burst of star formation some $\sim 10^5$ yr ago. *We regard this as the most likely possibility.* Furthermore, if the lifetime of the Class 0 phase is actually similar to that of the Class I phase, Class 0 protostars may not have such dramatically high accretion rates compared with Class I protostars, as has previously been assumed.

The lifetime of the starless cores found in this survey is similar to the $\sim 10^6$ yr derived from surveys using the lack of an *IRAS* association to define "starless" (e.g., Lee & Myers 1999). The cores therefore last only 2–3 free-fall times before collapsing. Temperatures of only $\sim$ 10–12 K are needed for the dominant support mechanism of the cores to be thermal pressure. The starless cores are therefore on the verge of collapse, and it is unlikely that strong magnetic fields are important for the collapse dynamics of the cores on scales $r \sim 10^4$ AU. Further work is needed to determine the velocity structure of these cores through molecular line spectroscopy.

The authors thank the staff of the JCMT for carrying out some of the ^{12}CO observations of the outflows in service observing mode. We also thank the anonymous referee for his/her careful reading of the text, and comments that have helped to clarify the paper. A.E.V. was supported by a Marie Curie Research Training Grant; J.S.R. and C.J.C. acknowledge the support of a Royal Society Fellowship and a PPARC Advanced Fellowship, respectively, during part of this work. The National Radio Astronomy Observatory is a facility of the National Science Foundation operated under cooperative agreement by Associated Universities, Inc. The James Clerk Maxwell Telescope (JCMT) is operated by the Joint Astronomy Centre on behalf of the Particle Physics and Astronomy Research Council of the United Kingdom, the Netherlands Organization for Scientific Research, and the National Research Council of Canada. The Digitized Sky Surveys were produced at the Space Telescope Science Institute under US Government grant NAG W-2166. The images of these surveys are based on photographic data obtained using the Oschin Schmidt Telescope on Palomar Mountain and the UK Schmidt Telescope. The plates were processed into the present compressed digital form with the permission of these institutions.

REFERENCES

Adams, F. C., Lada, C. J., & Shu, F. H. 1987, ApJ, 312, 788

André, P., & Montmerle, T. 1994, ApJ, 420, 837

André, P., Ward-Thompson, D., & Barsony, M. 1993, ApJ, 406, 122

André, P., Ward-Thompson, D., & Barsony, M., 2000, in Protostars and Planets IV, eds V. Mannings, A. P. Boss, & S. S. Russell (Tucson: University of Arizona Press), 59

André, P., Ward-Thompson, D., & Motte, F. 1996, A&A, 314, 625

Anglada, G., Sepulveda, I., & Gomez, J. F. 1997, A&AS, 121, 255

Armstrong, J. T., & Winnewisser, G. 1989, A&A, 210, 373

Bacmann, A., André, P., Puget, J.-L., Abergel, A., Bontemps, S., & Ward-Thompson, D. 2000, A&A, 361, 555

Barnard, E. E. 1927, Catalogue of 349 dark objects in the sky (Chicago: Univ. Chicago Press)

Basu, S., & Mouschovias, T. C. 1995, ApJ, 453, 271

Beichman, C. A., Myers, P. C., Emerson, J. P., Harris, S., Mathieu, R., Benson, P. J., & Jennings, R. E. 1986, ApJ, 307, 337

Benson, P. J., & Myers, P. C. 1989, ApJS, 71, 89

Bianchi, S., Davies, J. I., Alton, P. B., Gerin, M., & Casoli, F. 2000, A&A, 353, L13

Bohlin, R. C., Savage, B. D., & Drake, J. F. 1978, ApJ, 224, 132

Bontemps, S., André, P., Terebey, S., & Cabrit, S. 1996, A&A, 311, 858

Cabrit, S., & Bertout, C. 1992, A&A, 261, 274

Cabrit, S., Goldsmith, P. F., & Snell, R. L. 1988, ApJ, 334, 196

Chandler, C. J., & Richer, J. S. 2000, ApJ, 530, 851

Chen, H., Myers, P. C., Ladd, E. F., & Wood, D. O. S. 1995, ApJ, 445, 377

Chengalur, J. N., Lewis, B. M., Eder, J., & Terzian, Y. 1993, ApJS, 89, 189

Ciolek, G. E., & Mouschovias, T. Ch. 1994, ApJ, 425, 142

Clemens, D. P., & Barvainis, R. 1988, ApJS, 68, 257

Curiel, S., Raga, A., Raymond, J., Noriega-Crespo, A., & Cantó, J. 1997, AJ, 114, 2736

Dame, T. M., & Thaddeus, P. 1985, ApJ, 297, 751

Dame, T. M., et al. 1987, ApJ, 322, 706

de Geus, E. J. 1992, A&A, 262, 258

Dobashi, K., Bernard, J. P., Yonekura, Y., & Fukui, Y. 1994, ApJS, 95, 419

Emerson, D. T. 1995, in ASP Conf. Ser. 75, Multi-feed Systems for Radio Telescopes, ed. D. T. Emerson, & J. M. Payne (San Francisco: ASP), 309

Emerson, D. T., Klein, U., & Haslam, C. G. T. 1979, A&A, 76, 92

Evans, N. J., Rawlings, J. M. C., Shirley, Y. L., & Mundy, L. G. 2001, ApJ, 557, 193

Foster, P. N., & Chevalier, R. A. 1993, ApJ, 416, 303

Fuller, G. A., Lada, E. A., Masson, C. R., & Myers, P. C. 1995, ApJ, 453, 754

Hatchell, J., Fuller, G. A., & Ladd, E. F. 1999, A&A, 344, 687

Heitsch, F., Mac Low, M.-M., & Klessen, R. S. 2001, ApJ, 547, 280

Henning, Th., & Launhardt, R. 1998, A&A, 338, 223

Henning, Th., Michel, B., & Stognienko, R. 1995, Planet. Space Sci., 43, 1333

Henriksen, R., André, P., & Bontemps, S. 1997, A&A, 323, 549

Hildebrand, R. H. 1983, QJRAS, 24, 267

Hilton, J., & Lahulla, J. F. 1995, A&AS, 113, 325

Hodapp, K.-W. 1998, ApJ, 500, L183

Holland, W. S., et al. 1999, MNRAS, 303, 659

Huard, T. L., Sandell, G., & Weintraub, D. A. 1999, ApJ, 526, 833

Ichikawa, T., & Nishida, M. 1989, AJ, 97, 1074

Jayawardhana, R., Hartmann, L., & Calvet, N. 2001, ApJ, 548, 310

Jenness, T., & Lightfoot, J. F. 1998, in ASP Conf. Ser. 145, Astronomical Data Analysis Software and Systems VII, ed. R. Albrecht, R. N. Hook, & H. A. Bushouse (San Francisco: ASP), 216

Jenness, T., Lightfoot, J. F., & Holland, W. S. 1998, Proc. SPIE, 3357, 548

Jijina, J., Myers, P. C., & Adams, F. C. 1999, ApJS, 125, 161

Johnstone, D., & Bally, J. 1999, ApJ, 510, L49

Kenyon, S. J., Hartmann, L. W., Strom, K. M., & Strom, S. E. 1990, AJ, 99, 869

Lada, C. J., & Wilking, B. A. 1984, ApJ, 287, 610

Launhardt, R., & Henning, Th. 1997, A&A, 326, 329

Launhardt, R., Ward-Thompson, D., & Henning, Th. 1997, MNRAS, 288, L45

Lee, C. W., & Myers, P. C. 1999, ApJS, 123, 233

Leung, C. M., Kutner, M. L., & Mead, K. N. 1982, ApJ, 262, 583

Li, P. S., Norman, M. L., Heitsch, F., & Mac Low, M.-M. 2000, BAAS, 32, 1393

Lynds, B. T. 1962, ApJS, 7, 1

McLaughlin, D. E., & Pudritz, R. E. 1997, ApJ, 476, 750

Moriarty-Schieven, G. H., & Snell, R. L. 1989, ApJ, 338, 952

Motte, F., & André, P. 2001, A&A, 365, 440

Motte, F., André, P., & Neri, R. 1998, A&A, 336, 150

Myers, P. C., Fuller, G. A., Mathieu, R. D., Beichman, C. A., Benson, P. J., Schild, R. E., & Emerson, J. P. 1987, ApJ, 319, 340

Myers, P. C., Heyer, M., Snell, R., & Goldsmith, P. 1988, ApJ, 324, 907

Myers, P. C., & Ladd, E. F. 1993, ApJ, 413, L47

Myers, P. C., Linke, R. A., & Benson, P. J. 1983, ApJ, 264, 517

Nozawa, S., Mizuno, A., Teshima, Y., Ogawa, H., & Fukui, Y. 1991, ApJS, 77, 647

Ossenkopf, V., & Henning, Th. 1994, A&A, 291, 943

Parker, N. D. 1988, MNRAS 235, 139

Parker, N. D. 1989, PhD thesis, Univ. Cambridge

Parker, N. D. 1991, MNRAS, 251, 63

Parker, N. D., Padman, R., & Scott, P. F. 1991, MNRAS, 252, 442

Robert, C., & Pagani, L. 1993, A&A, 271, 282

Shirley, Y. L., Evans, N. J., Rawlings, J. M. C., & Gregersen, E. M. 2000, ApJS, 131, 249

Shu, F. H. 1977, ApJ, 214, 488

Tafalla, M., Myers, P. C., Mardones, D., & Bachiller, R. 2000, A&A, 359, 967

Tapia, M., Persi, P., Bohigas, J., & Ferrari-Toniolo, M. 1997, AJ, 113, 1769

Tomita, Y., Saito, T., & Ohtani, H. 1979, PASJ, 31, 407

Visser, A. E. 2000, PhD thesis, Univ. Cambridge

Visser, A. E., Richer, J. S., & Chandler, C. J. 2001, MNRAS, 323, 257 (Paper I)

Ward-Thompson, D., Motte, F., & André, P. 1999, MNRAS, 305, 143

Ward-Thompson, D., Scott, P. F., Hills, R. E., & André, P. 1994, MNRAS, 268, 276

Wilking, B. A., Lada, C. J., & Young, E. T. 1989, ApJ, 340, 823

Williams, J. P., Blitz, L., & McKee, C. F. 2000, in Protostars and Planets IV, ed. V. Mannings, A. P. Boss, & S. S. Russell (Tucson: Univ. Arizona Press), 97

Yonekura, Y., Dobashi, K., Mizuno, A., Ogawa, H., & Fukui, Y. 1997, ApJS, 110, 21

This preprint was prepared with the AAS LATEX macros v5.0.

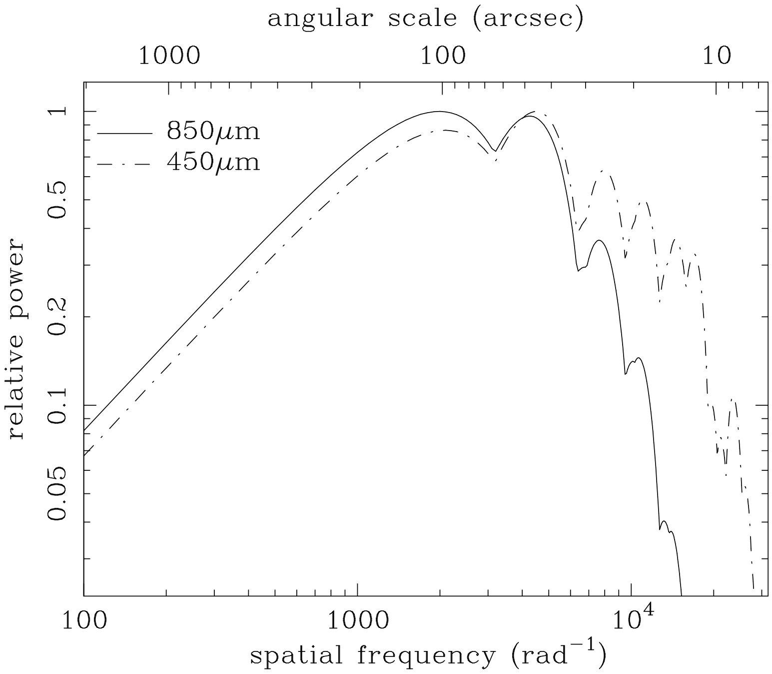

Fig. 1.— Spatial frequency coverage of scan maps made using the Emerson2 technique, with chop throws of 20″, 30″, and 65″. It has been calculated by adding the moduli of the FT of the three dual beam functions. The solid line shows the 850 μm coverage, and the dot-dashed line the 450 μm coverage. Low spatial frequencies are measured (apart from zero frequency) but with less sensitivity than the higher spatial frequencies and can result in spatially extended noise features in the scan maps.

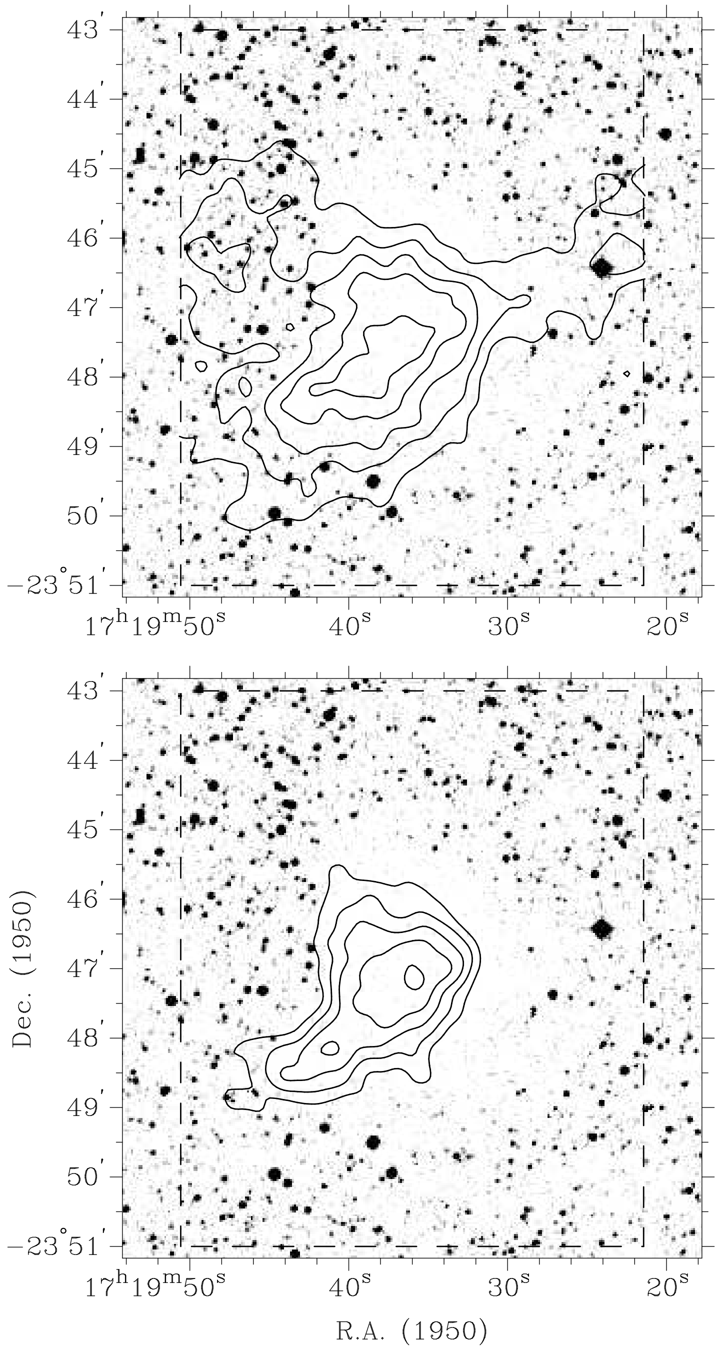

Fig. 2.— Deep SCUBA images of L57 (B68) at 450 μm (top) and 850 μm (bottom). The *IRAS* source associated with this cloud by Launhardt & Henning (1997) is 2′ south of the cloud and is not covered by the SCUBA map. The 450 μm contour levels are at 3σ, 4.5σ, 6σ, 7.5σ, and 9σ (σ = 67 mJy beam^{-1}). The 850 μm contour levels are at 1σ, 2σ, 3σ, 4σ, and 5σ with σ = 14 mJy beam^{-1}.

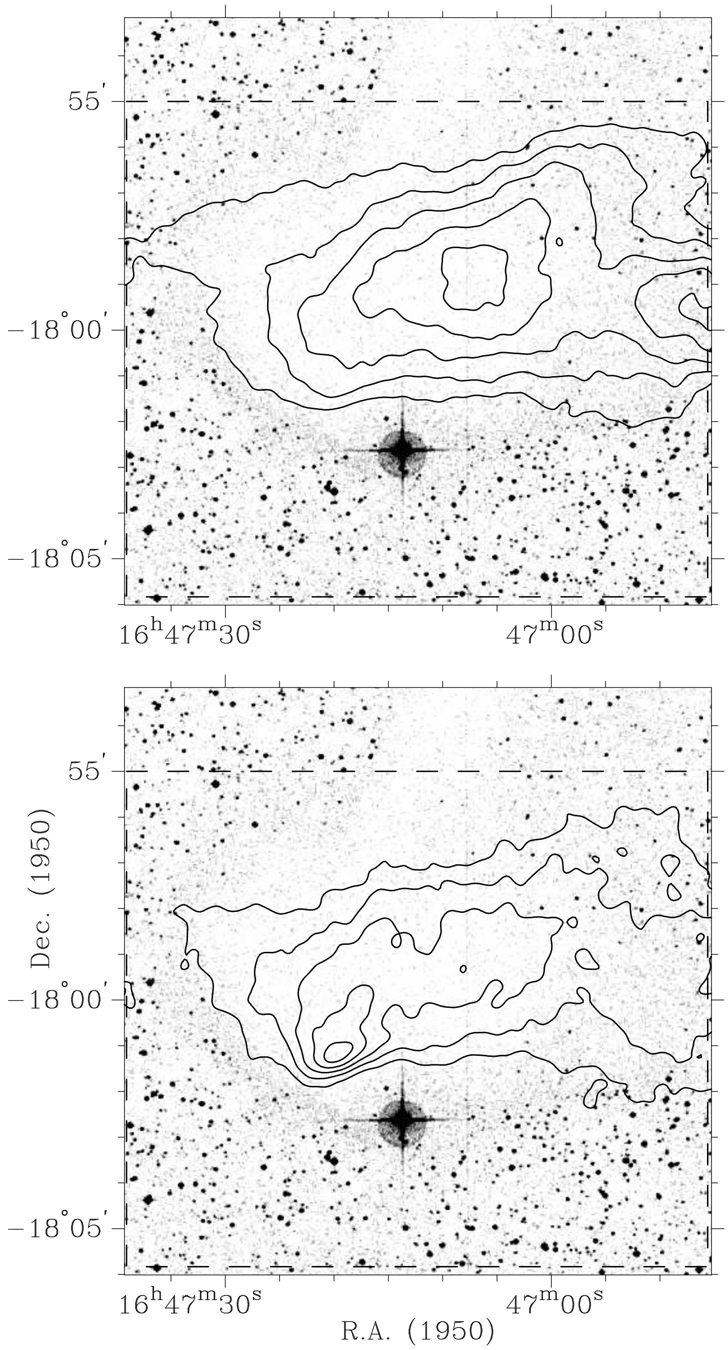

Fig. 3.— L63 contains a well-known starless core (Ward-Thompson et al. 1994; Ward-Thompson, Motte, & André 1999) in the southeast part of the cloud, detected here at 850 μm (*bottom*) but not at 450 μm (*top*). Extended emission is detected at both wavelengths. No *IRAS* sources are associated with this cloud. Both the 450 μm and 850 μm contour levels are at 1σ, 2σ, 3σ, 4σ, and 5σ, with $\sigma_{450} = 335$ mJy beam^{-1} and $\sigma_{850} = 38$ mJy beam^{-1}.

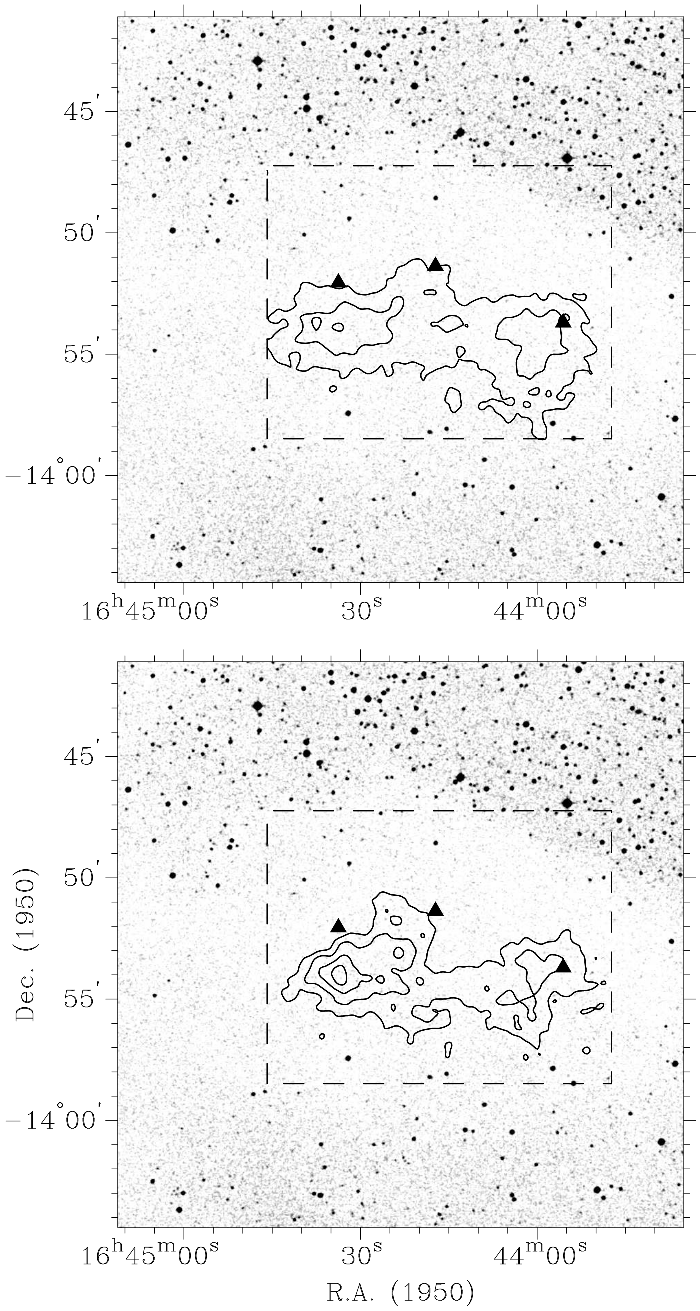

Fig. 4.— Extended emission is detected from L158 at both 450 μm (*top*) and 850 μm (*bottom*). Three *IRAS* sources are covered by the SCUBA map (*triangles*), but none of these can be associated with submillimeter emission. IRAS 16445−1352 is not a Class I object as sometimes quoted but is cirrus (Beichman et al. 1986; Bontemps et al. 1996). The other two *IRAS* sources are both only detected at 60 μm and could also be cirrus. The 450 μm contour levels are at 1σ, 2σ, and 3σ ($\sigma = 268$ mJy beam^{-1}). The 850 μm contour levels are at 1σ, 2σ, 3σ, and 4σ ($\sigma = 24$ mJy beam^{-1}).

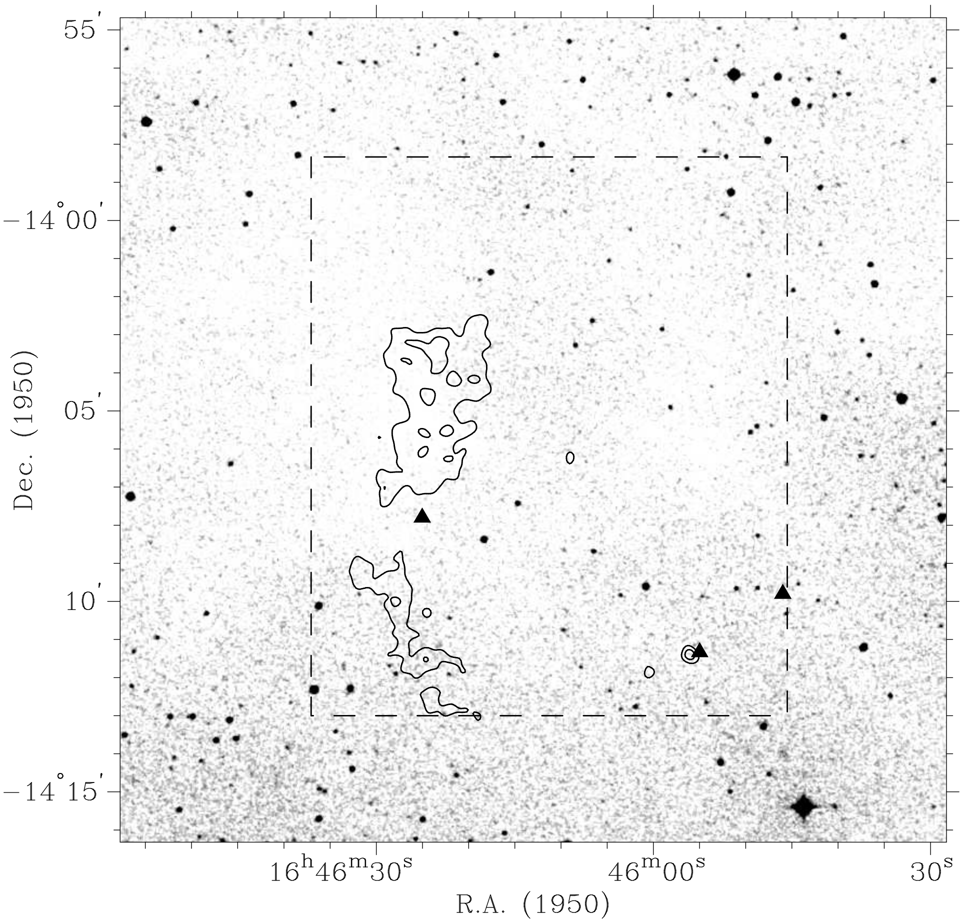

Fig. 5.— Central region of L162 mapped during weather conditions suitable only for observing at 850 μm. Three *IRAS* sources were covered by the SCUBA map (*triangles*). Emission from the T Tauri star IRAS 16459−1411 has been detected (*bottom right*), but the other two *IRAS* sources are not detected, and may be cirrus. The contour levels are at 5σ and 7σ (with $\sigma = 20$ mJy beam^{-1}). Although the extended emission at the top of the map correlates well with the dark cloud, the bottom part does not, which may indicate problems with the baseline subtraction.

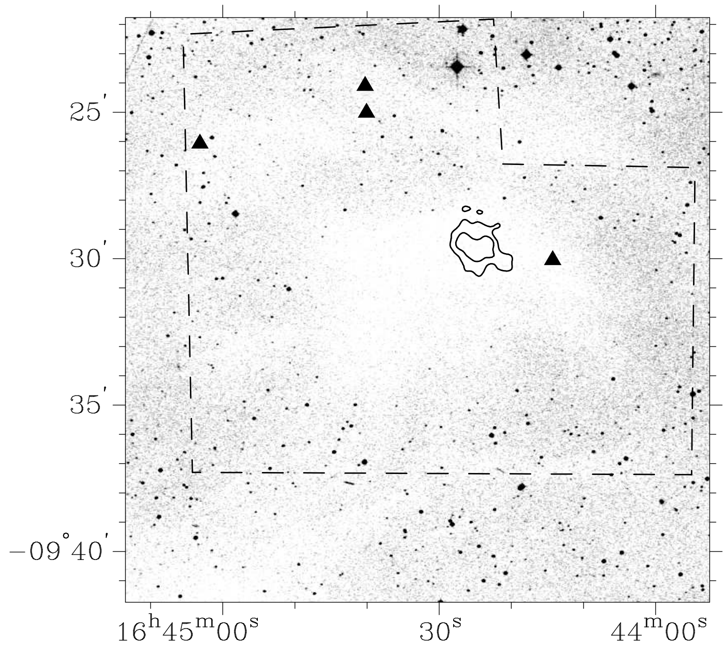

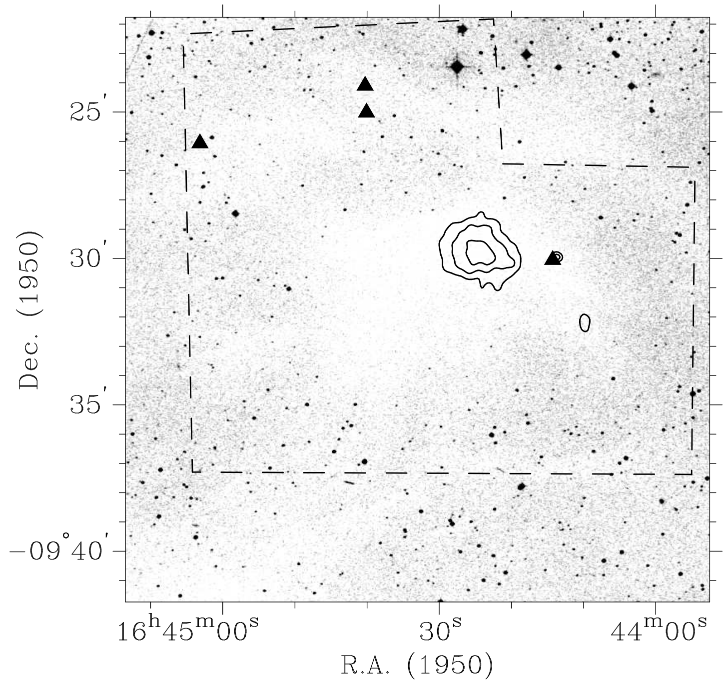

Fig. 6.— L260 contains a well-known Class I protostar detected at 850 μm (*bottom*) but not at 450 μm (*top*). A further three *IRAS* sources (*triangles*) are covered by the SCUBA map, but none was detected. There is also extended emission east of the protostar at both wavelengths. The 450 μm contour levels are at 1σ and 2σ ($\sigma = 134$ mJy beam^{-1}). The 850 μm contour levels are at 1σ, 2σ, and 3σ ($\sigma = 24$ mJy beam^{-1}).

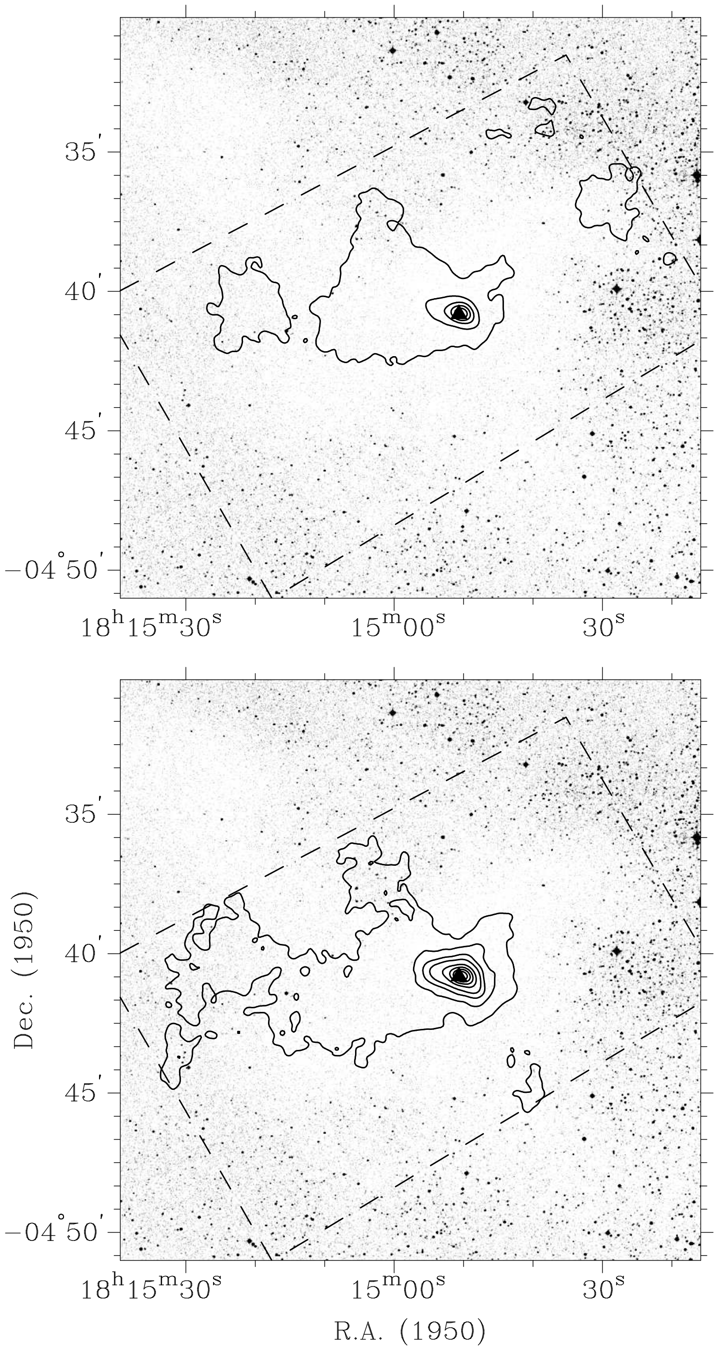

Fig. 7.— L483 contains a well-known protostar clearly detected at both 450 μm (*top*) and 850 μm (*bottom*). Extended dust emission is also detected and appears to outline the outflow from the central source. The 450 μm contour levels are at 1σ, 3σ, 5σ, 7σ, 9σ, and 11σ ($\sigma = 355$ mJy beam^{-1}), and the 850 μm contour levels are at 1σ, 4σ, 7σ, 10σ, 16σ, 22σ, 28σ, 34σ, and 40σ, with $\sigma = 22$ mJy beam^{-1}.

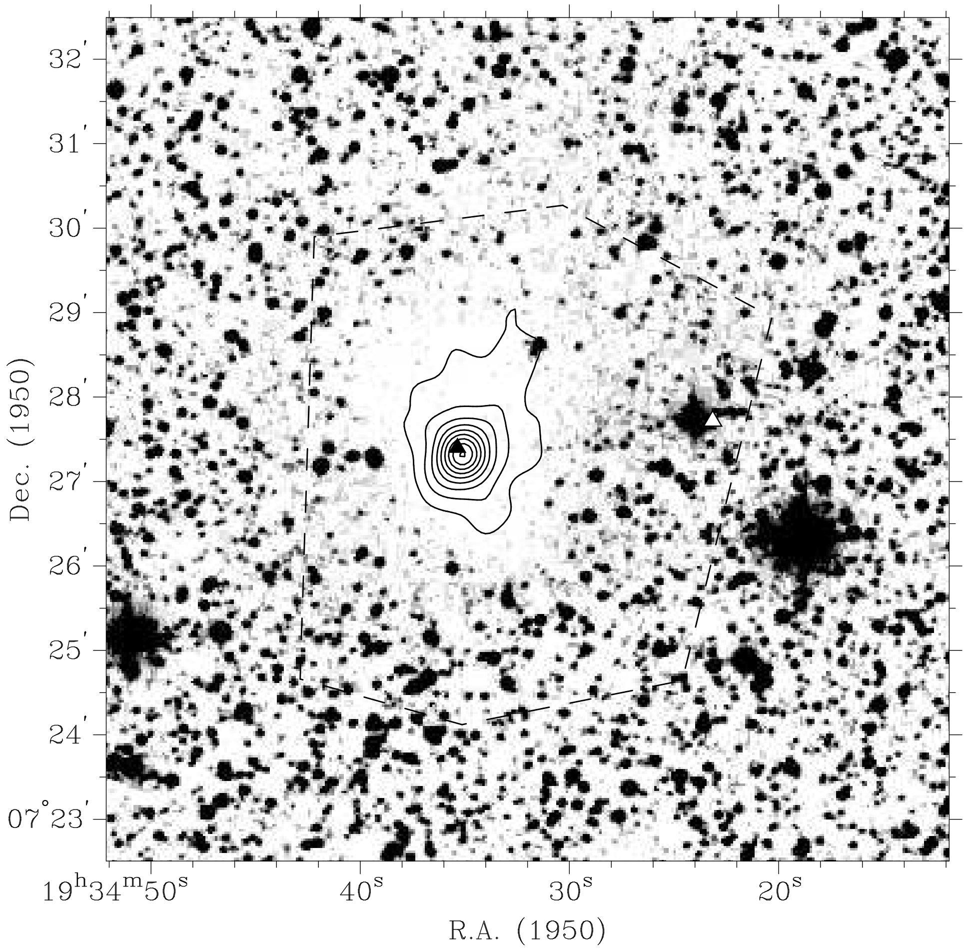

Fig. 8.— L663 (B335) is the most famous cloud in this sample. It has been imaged using the EKH technique at 850 μm. Strong submillimeter emission originates from a Class 0 protostar that has been identified with the *IRAS* source 19345+0727 (*triangle*). A second *IRAS* source to the west, also covered by the SCUBA map but not detected in the submillimeter, is associated with a bright star. The 850 μm contour levels are at 1σ, 2σ, 3σ, 4σ, 5σ, 6σ, 7σ, 8σ, and 9σ ($\sigma = 74$ mJy beam^{-1}).

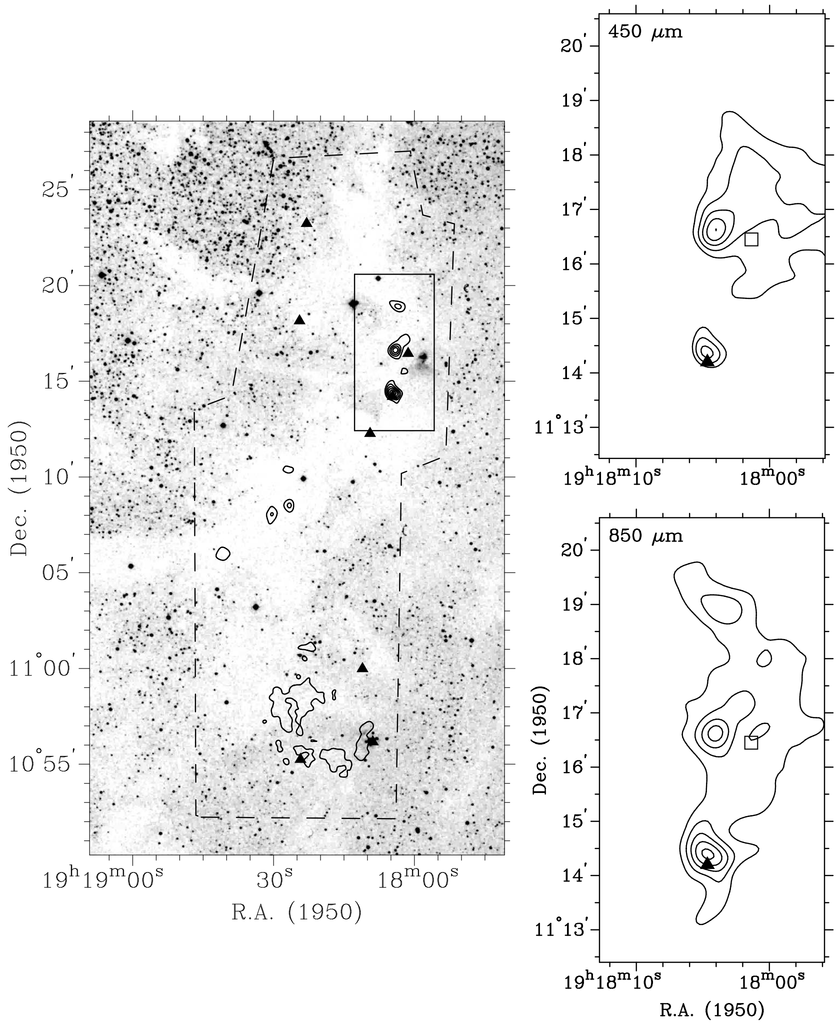

Fig. 9.— *Left:* Overlay of 850 μm contours on the optical image of L673. Some extended emission is detected towards the southern part of the cloud, although it does not correlate very well with the dust extinction. Eight *IRAS* sources are covered by this SCUBA map (*triangles*), but most have not been detected (e.g., the T Tauri star IRAS 19181+1056). The box indicates the area displayed in more detail on the right. This northern region is the only part mapped in both 450 and 850 μm. The 850 μm contours are at 2σ, 3σ, 4σ, 5σ, and 6σ (σ = 40 mJy beam^{-1}). *Right:* The submillimeter cores in the northern part of L673. IRAS 19180+1114 can be associated with the continuum source furthest south in this ridge (*triangle*). The submillimeter source north of 19180+1114 may be associated with 19180+1116 (*square*, see § 5.1) suggesting both could be protostars. The 450 μm contour levels are at 2σ, 3σ, 4σ, 5σ, and 6σ (σ = 147 mJy beam^{-1}). The 850 μm contours are at 1σ, 3σ, 5σ, 7σ, and 9σ (σ = 28 mJy beam^{-1}).

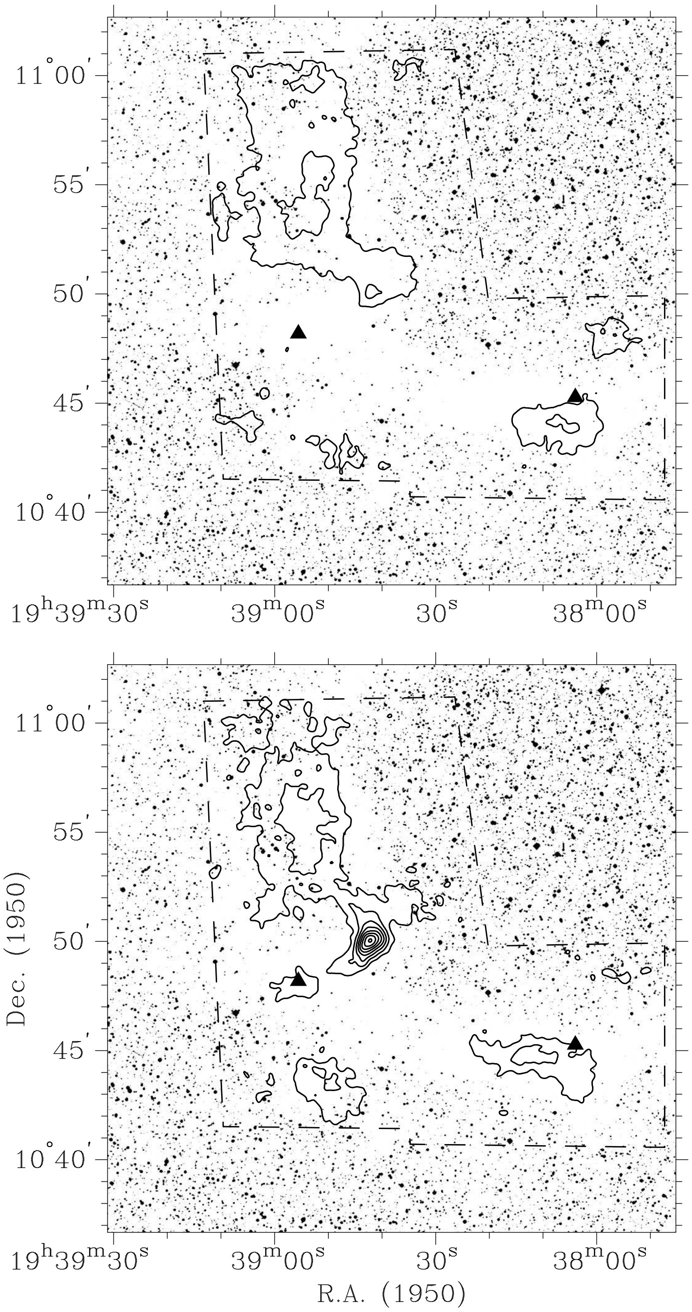

Fig. 10.— L694 contains a bright embedded submillimeter continuum source, clearly detected at 850 μm (*bottom*) but not at 450 μm (*top*). Extended emission is detected at both wavelengths and correlates well with the optical dust extinction. The maps cover two *IRAS* sources, but neither has been detected. IRAS 19389+1048 is probably cirrus, and IRAS 19380+1045 is very likely a (young) field star. The 450 μm contour levels are at 1σ and 2σ (σ = 201 mJy beam^{-1}). The 850 μm contour levels are at 1σ, 2σ, 3σ, 4σ, 5σ, 6σ, 7σ, and 8σ (σ = 25 mJy beam^{-1}).

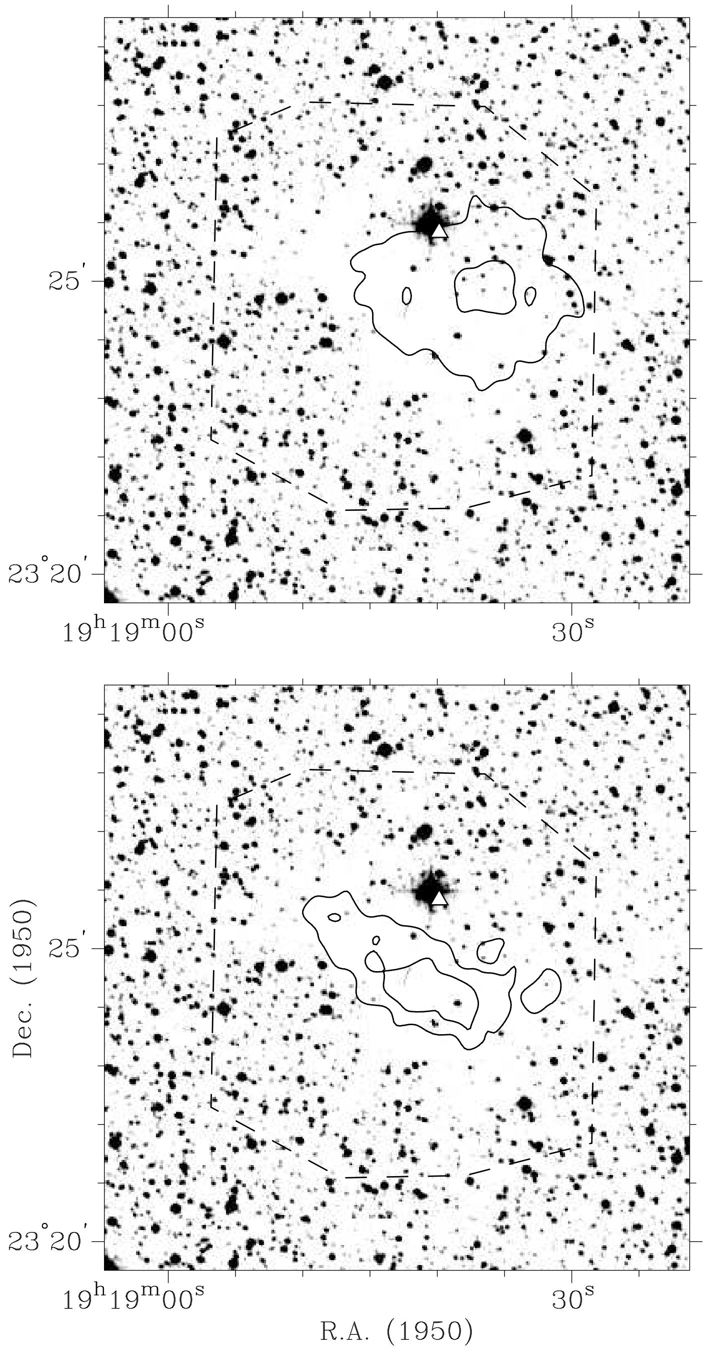

Fig. 11.— Extended emission has been detected from L771 at both 450 μm (*top*) and 850 μm (*bottom*) and appears different at the two wavelengths. The *IRAS* source in this field can probably be associated with the bright star (*triangle*). The 450 μm contours are at 3σ and 6σ ($\sigma = 100$ mJy beam^{-1}). The 850 μm contours are at 3σ and 4σ ($\sigma = 20$ mJy beam^{-1}).

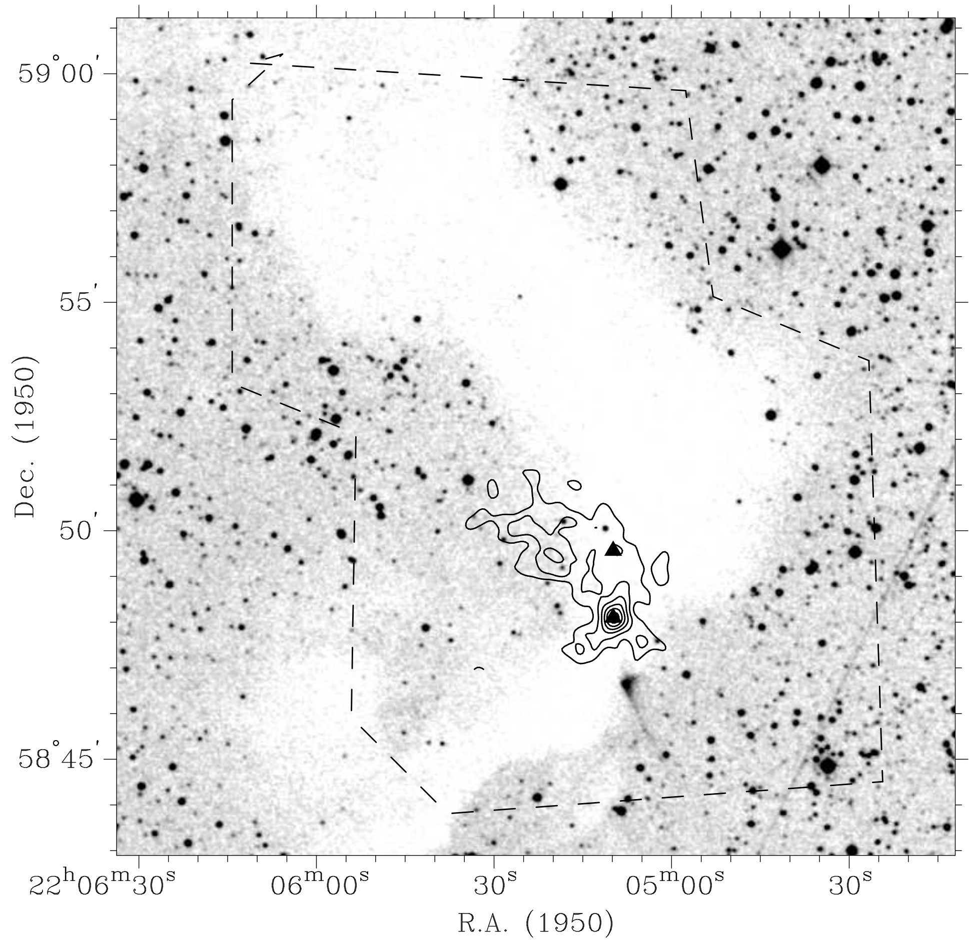

Fig. 12.— The 850 μm map of L1165 shows clearly the known protostar IRAS 22051+5848. The other *IRAS* source covered by this map is not detected and is probably a field star or T Tauri star. The contour levels are at 1σ, 2σ, 3σ, 4σ, 5σ, and 6σ (σ = 67 mJy beam^{-1}).

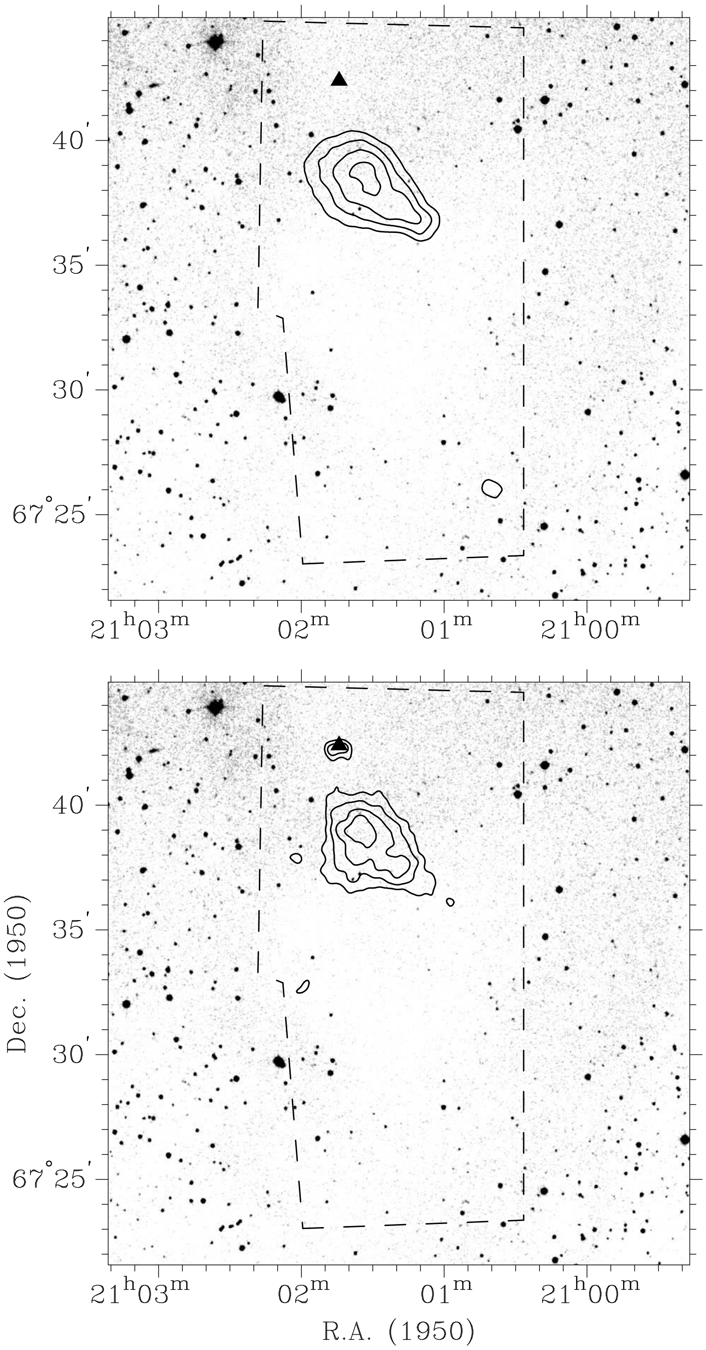

Fig. 13.— L1172 shows a compact continuum source at 850 μm (*bottom*) that coincides with IRAS 21017+6742 (*triangle*) and some extended emission detected at both 450 μm (*top*) and 850 μm. The 450 μm contour levels are at 2σ, 3σ, 4σ, and 5σ ($\sigma = 369$ mJy beam^{-1}, top image). The 850 μm contour levels are at also at 2σ, 3σ, 4σ, and 5σ ($\sigma = 22$ mJy beam^{-1}).

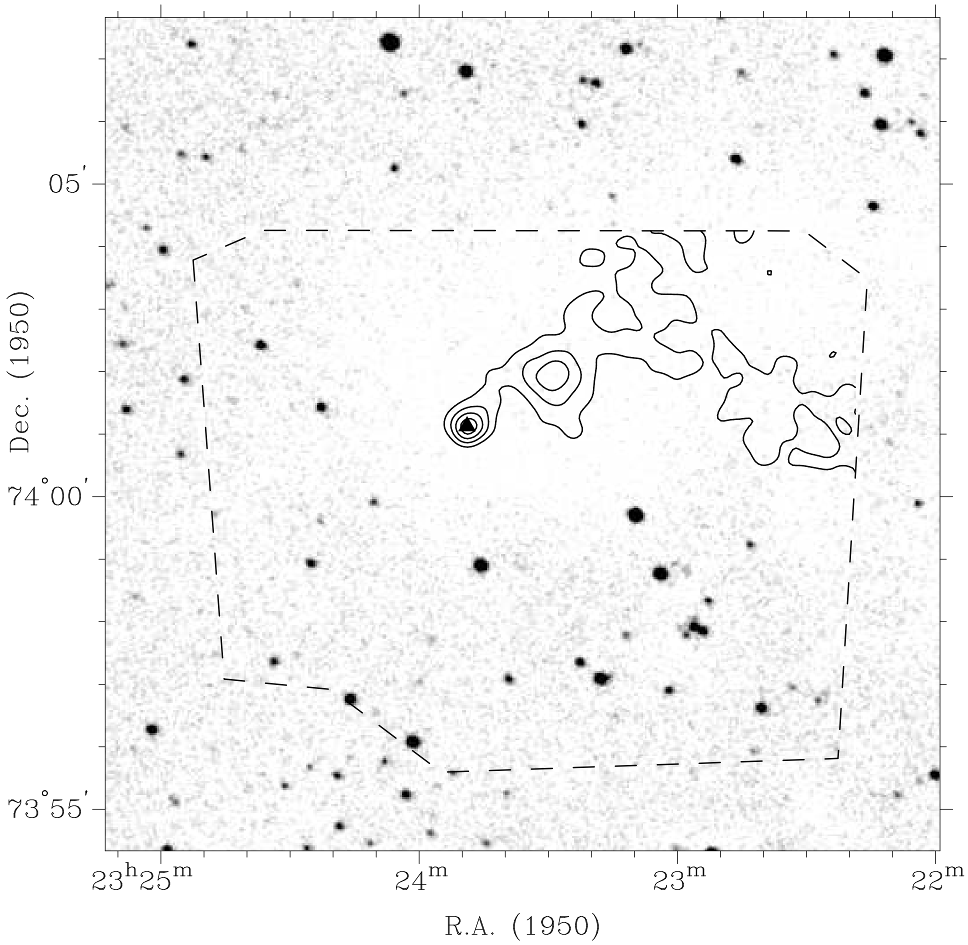

Fig. 14.— L1262 (CB244) contains a protostar, IRAS 23238+7401, that is clearly detected at 850 μm (*triangle*). The contour levels are at 3σ, 5σ, 7σ, and 9σ ($\sigma = 30$ mJy beam^{-1}).

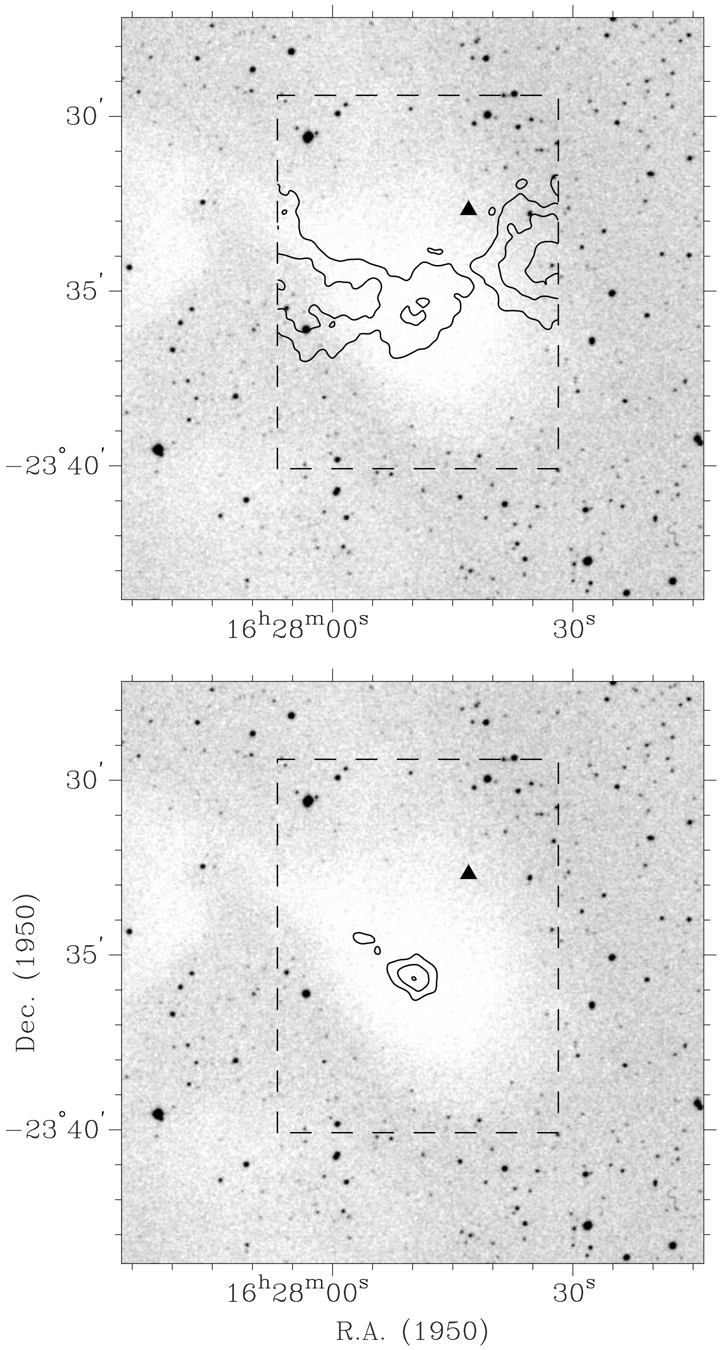

Fig. 15.— L1704 is associated with a continuum source most clearly detected at 850 μm (*bottom*) but also seen at 450 μm (*top*). IRAS 16277−2332 is covered by this map but is undetected. Both the 450 μm and the 850 μm contours are at 1σ, 2σ, and 3σ ($\sigma_{450} = 134$ mJy beam^{-1}, $\sigma_{850} = 18$ mJy beam^{-1}).

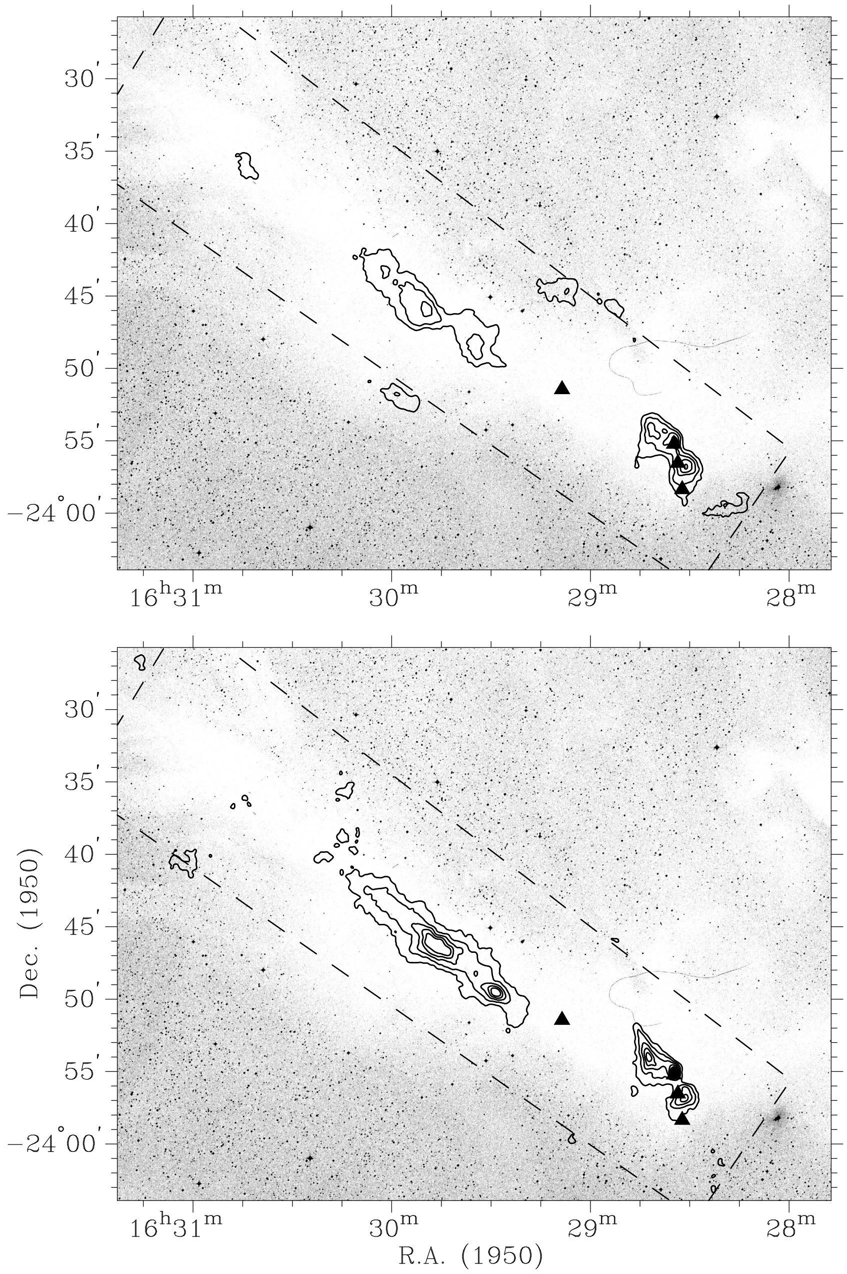

Fig. 16.— Extended continuum emission and compact sources are detected from L1709 at both 450 μm (*top*) and 850 μm (*bottom*). There are four *IRAS* sources in this cloud (*triangles*). The protostar IRAS 16285−2355 can be clearly associated with a submillimeter continuum source. South of this protostar, IRAS 16285−2356 is very close to another compact continuum source. The other two *IRAS* sources are not associated with submillimeter emission. The 450 μm contour levels are at 4σ, 6σ, 8σ, 10σ, and 12σ ($\sigma = 134$ mJy beam^{-1}), and the 850 μm contours are at 2σ, 4σ, 6σ, 8σ, 10σ, 14σ, 18σ, and 22σ with $\sigma = 20$ mJy beam^{-1}.

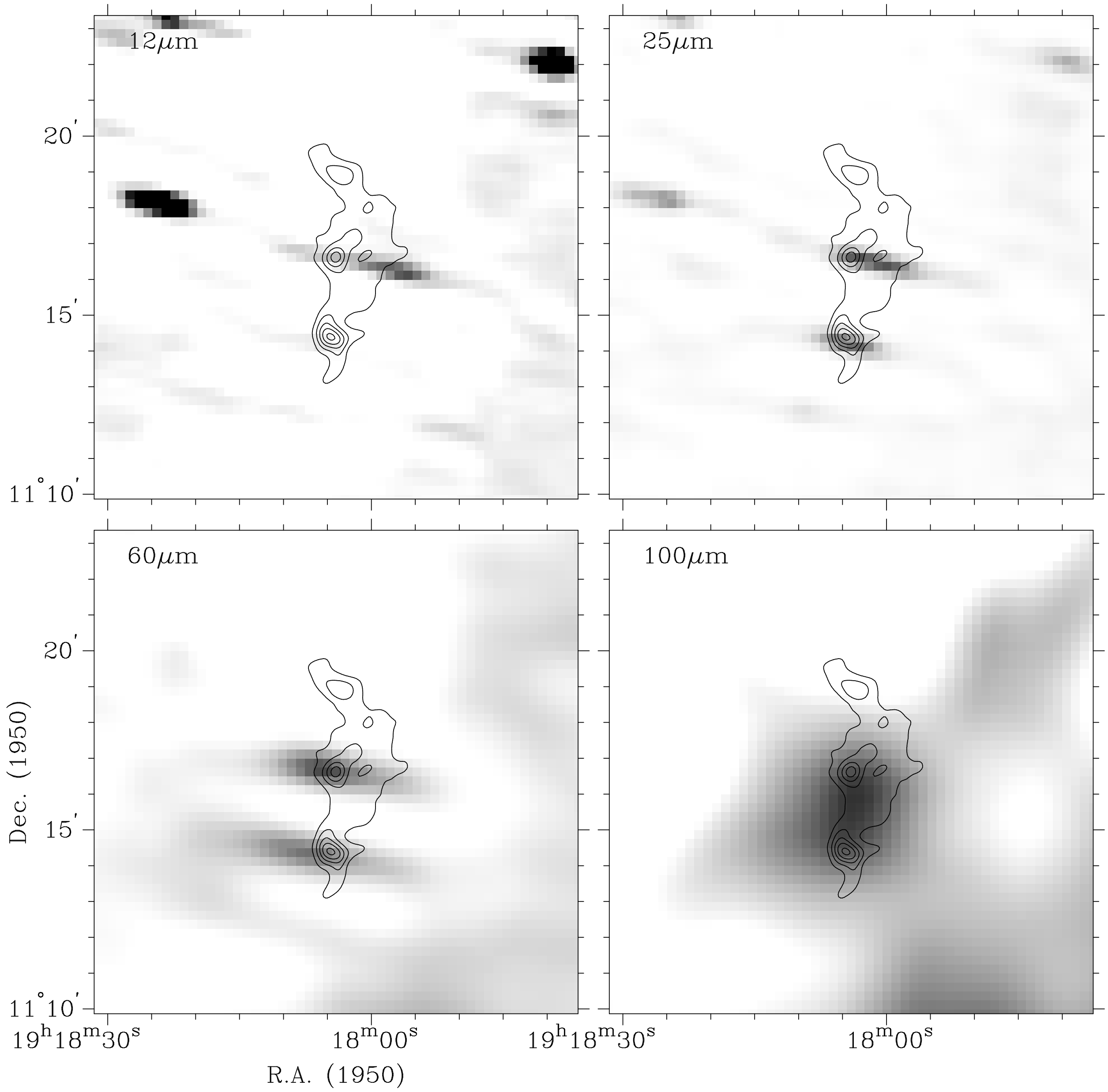

Fig. 17.— Contours of the 850 μm emission from L673 overlaid on HIRES-processed *IRAS* images in gray scale.

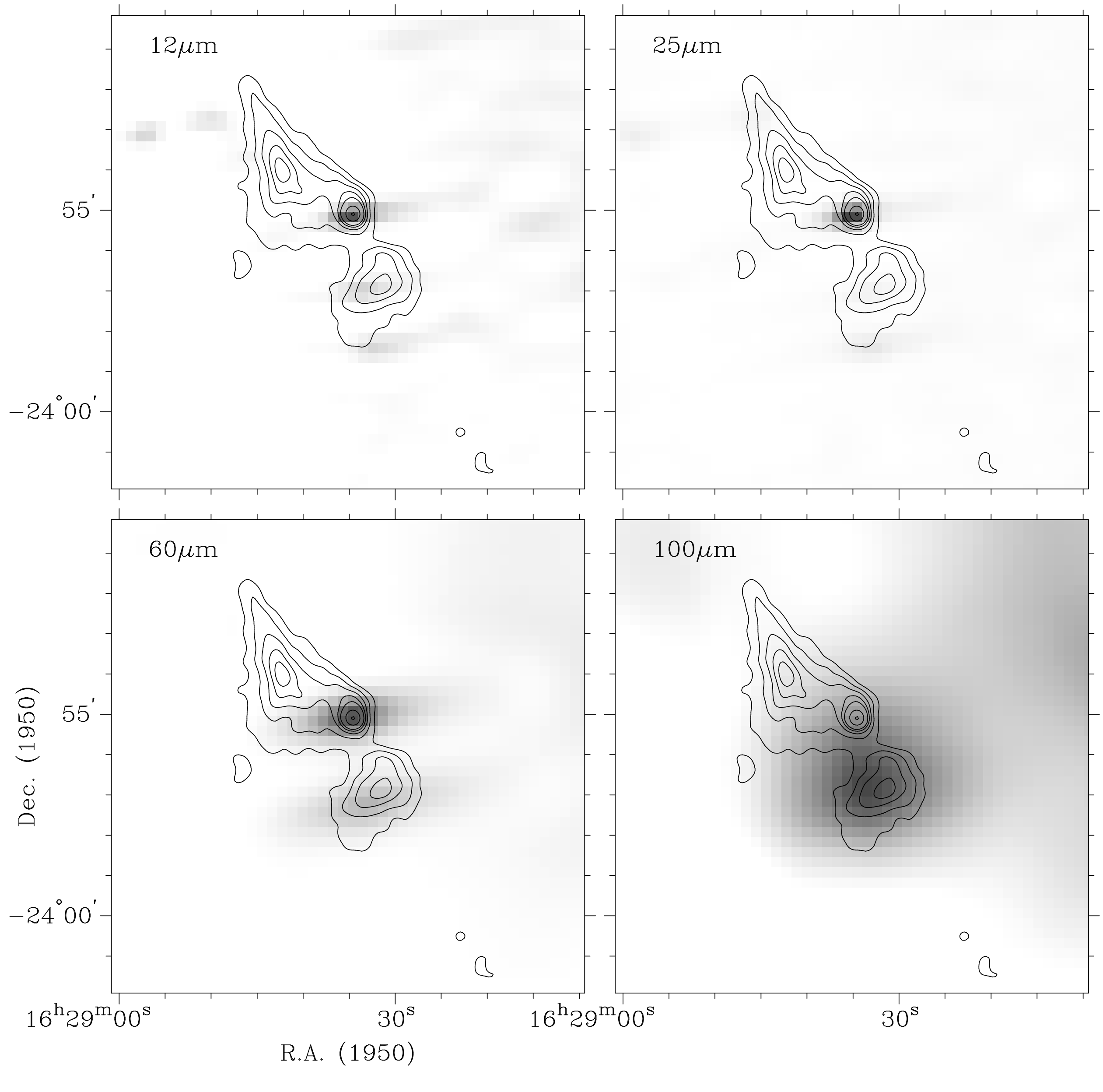

Fig. 18.— Contours of the 850 μm emission from L1709 overlaid on HIRES-processed *IRAS* images in gray scale. The most southern *IRAS* source visible in the 12 μm and 25 μm bands is 16285−2358, a known star (Ichikawa & Nishida 1989).

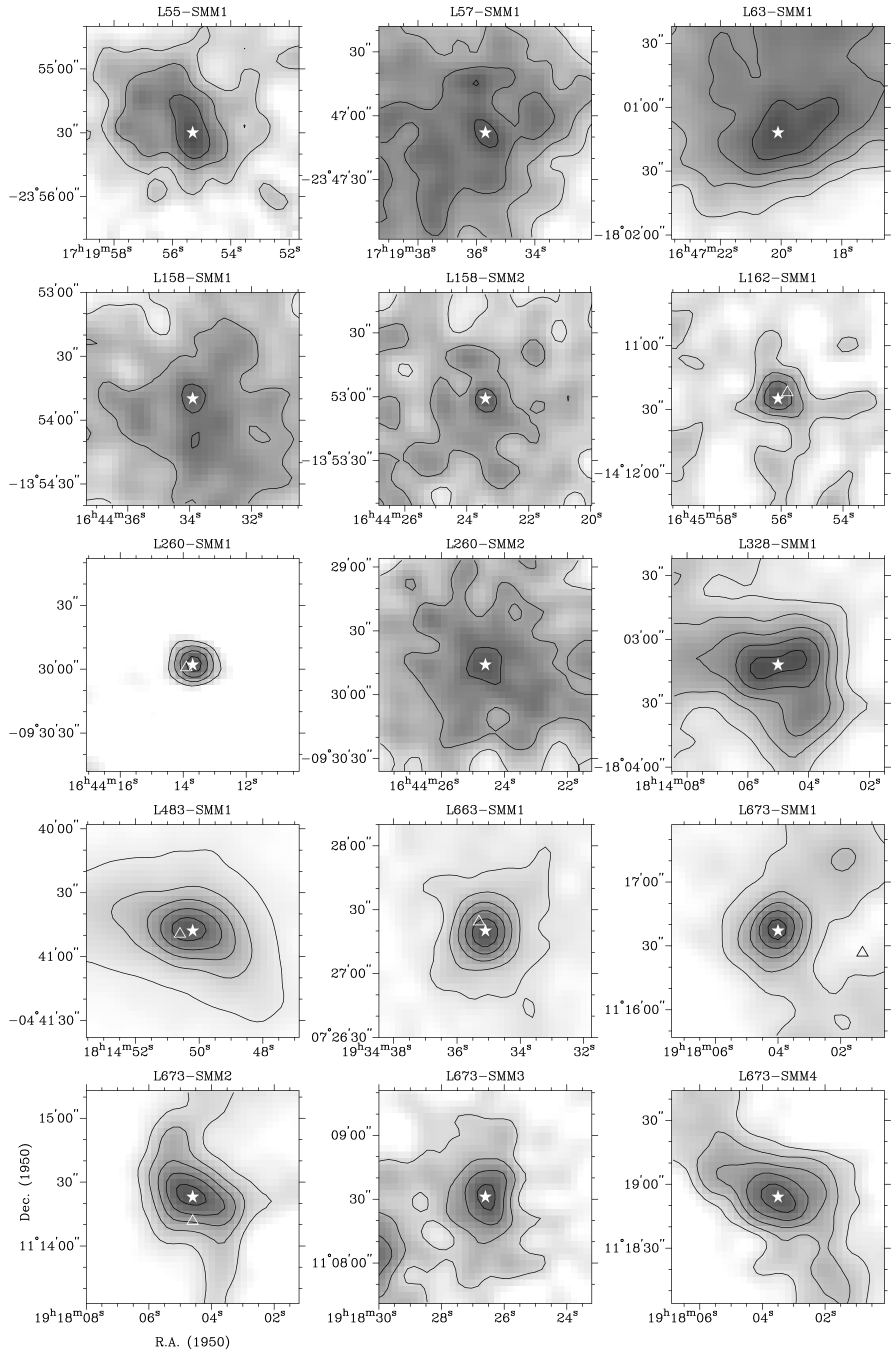

Fig. 19.— Images of all 40 submillimeter cores identified in the sample of Lynds dark clouds. Contours show the 850 μm emission, the positions in Table 4 are represented by stars, and triangles represent *IRAS* sources from the PSC.

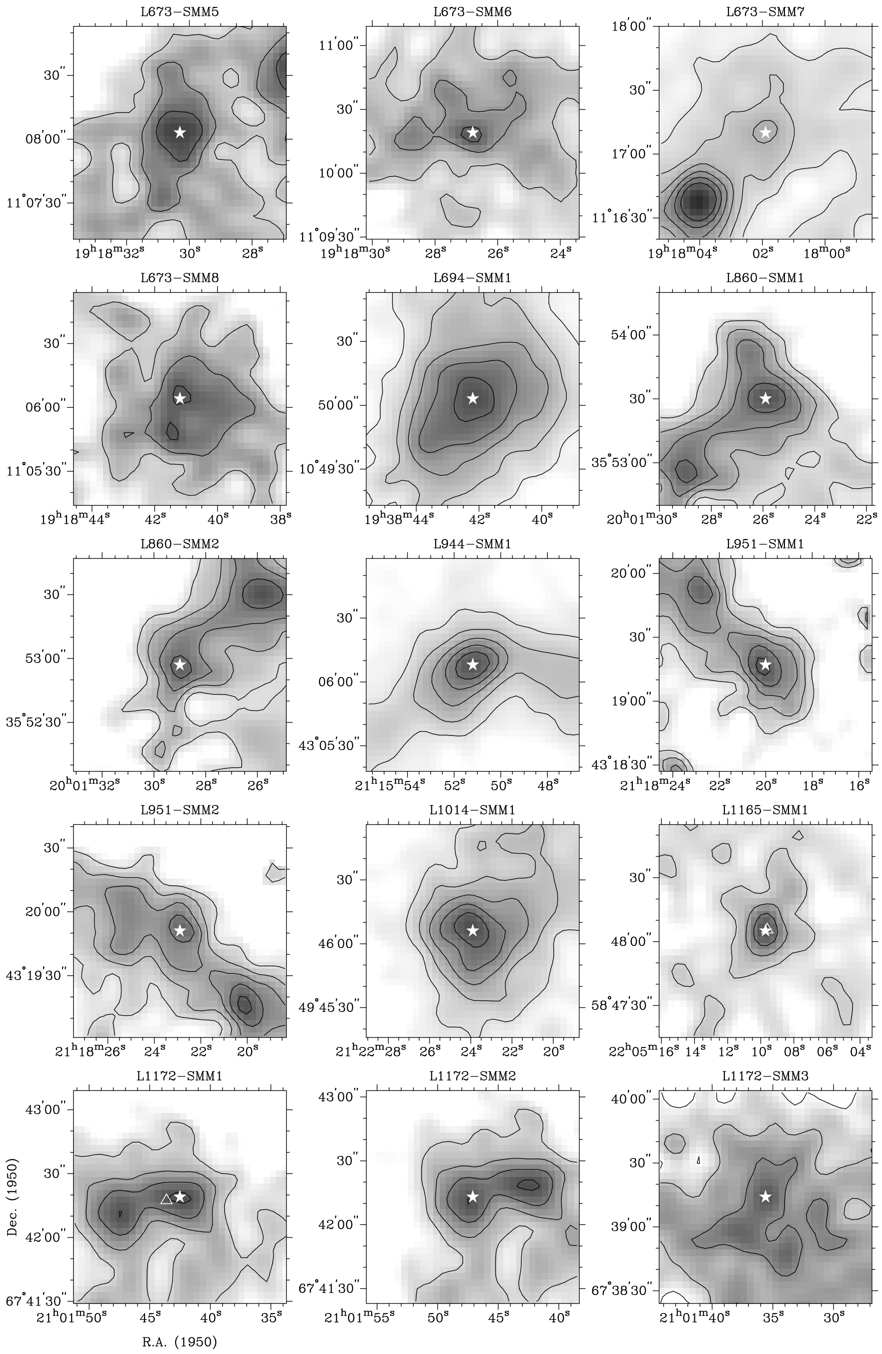

Fig. 19.— Continued.

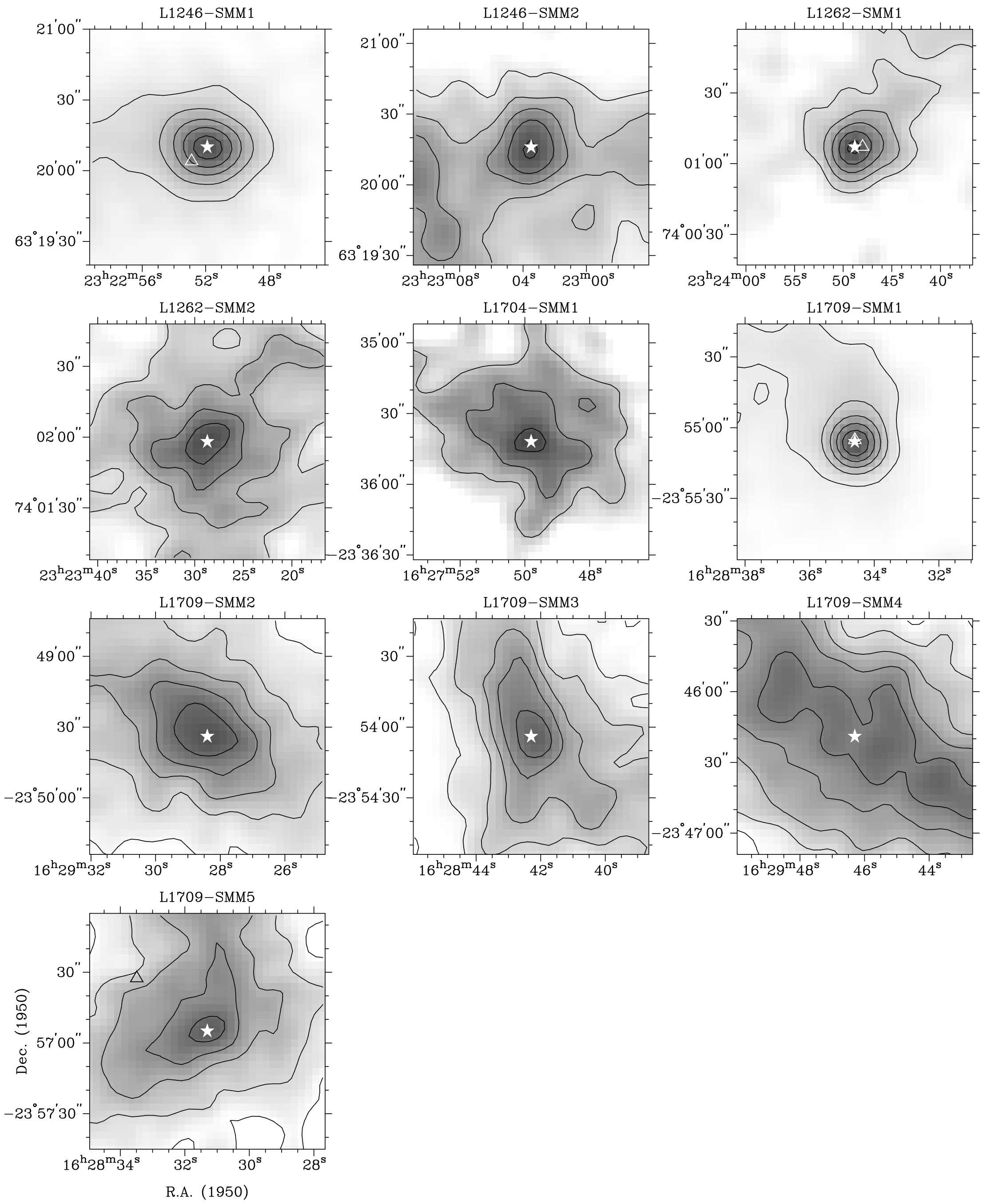

Fig. 19.— Continued.

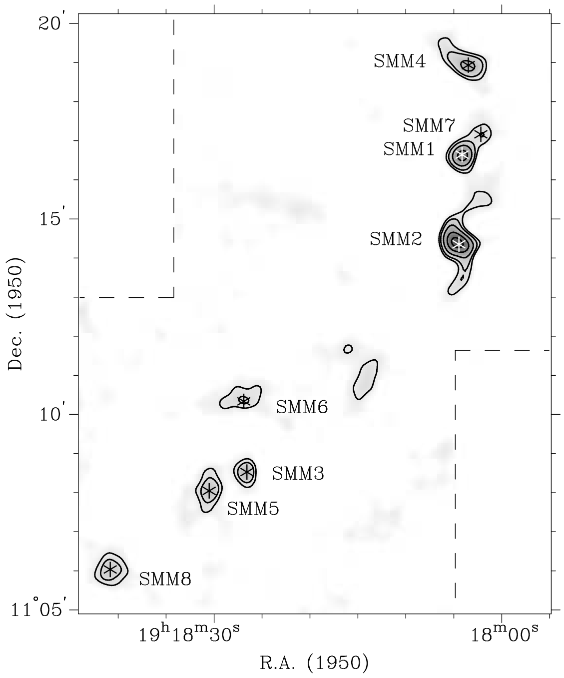

Fig. 20.— Positions of the compact submillimeter cores in L673 from Table 4 (*asterisks*) marked on the 850 μm SCUBA image.

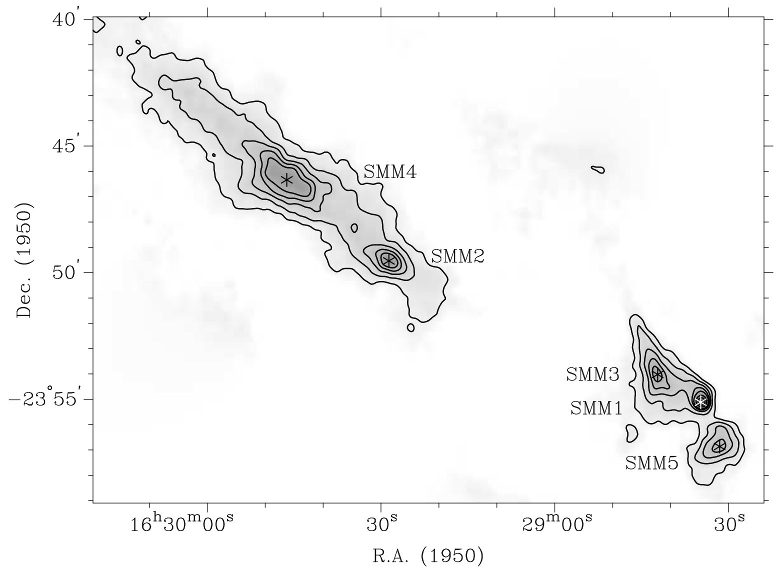

Fig. 21.— Same as Fig. 20, but for L1709.

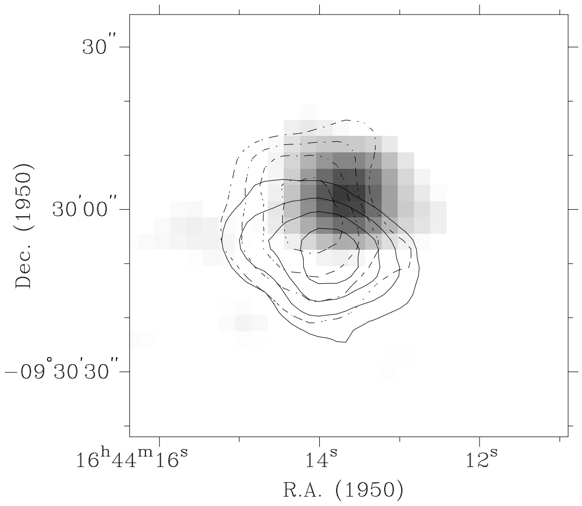

Fig. 22.— Outflow in L260. Redshifted gas is integrated over the LSR velocity range 4.5 to 7.5 km s^{-1} with contours of $\int T_A^* dV$ at 0.5 + 0.2n K km s^{-1}, where n = 1, 2, 3,..., and the blueshifted gas is integrated over the range −0.5 to 2.5 km s^{-1} with contours of $\int T_A^* dV$ at 0.4 + 0.2n K km s^{-1}. The contours are overlaid on a gray scale of the SCUBA 850 μm image.

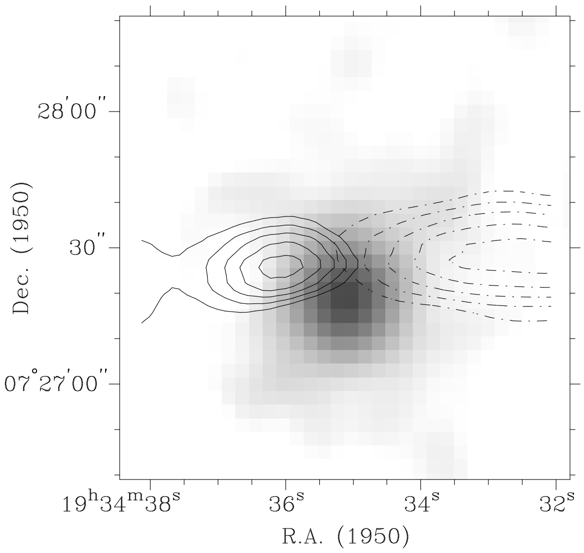

Fig. 23.— Outflow in L663. Redshifted gas is integrated over the LSR velocity range 11.5 to 22.0 km s^{-1} with contours of $\int T_A^* dV$ at 2.0 + 1.0n K km s^{-1}, where n = 1, 2, 3,..., and the blueshifted gas is integrated from −5.0 to 5.5 km s^{-1} with contours at 3.0 + 0.5n K km s^{-1}. The contours are overlaid on the SCUBA 850 μm image.

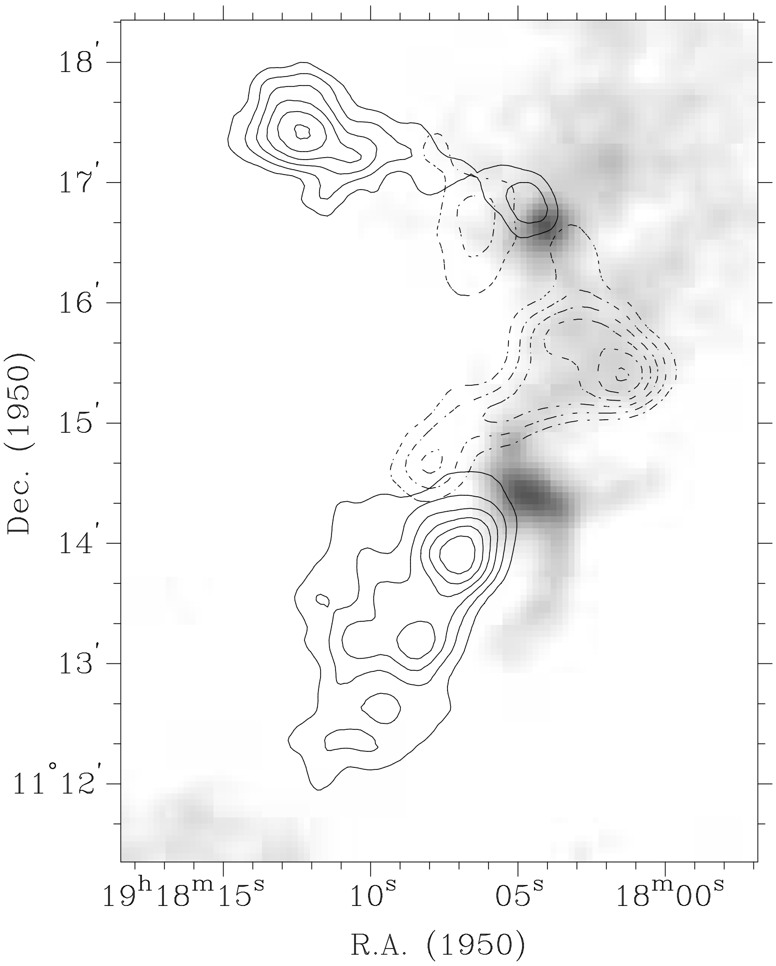

Fig. 24.— Blueshifted outflows are clearly detected from both submillimeter cores in L673, the outflow from L673−SMM1 in the northeast, and the outflow from L673−SMM2 directed toward the southeast. It is less clear which source is responsible for the redshifted flow. The blueshifted gas is integrated between $V_{\rm LSR}$ = −2.0 to 3.0 km s^{-1}. Contours of the blueshifted flow from L673−SMM1 (*top*) are at 0.7 + 0.4n K km s^{-1}, and for L673−SMM2 (*bottom*), they are at 2.0 + 1.0n K km s^{-1}. The redshifted gas is integrated from 9.0 to 15.0 km s^{-1} with contours at 7.0 + 2.0n K km s^{-1}. The contours are overlaid on the SCUBA 850 μm image.

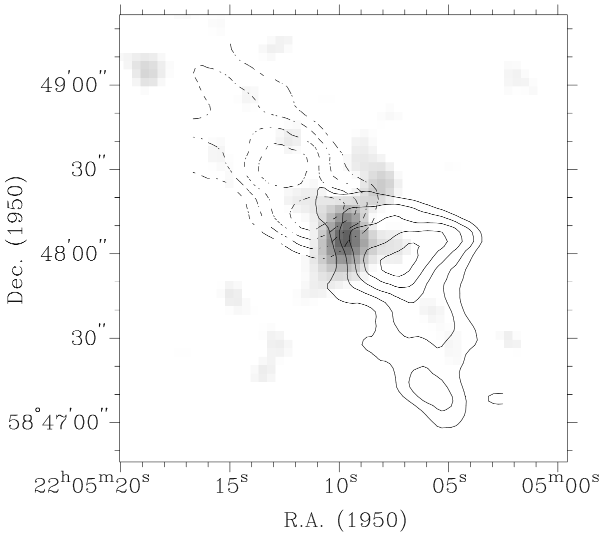

Fig. 25.— Outflow in L1165. Redshifted gas is integrated over the LSR velocity range -1.0 to 2.7 km s^{-1} with contours at 2.6 + 0.7n K km s^{-1}, and the blueshifted gas is integrated from -6.0 to -3.2 km s^{-1} with contours at 1.5 + 0.3n K km s^{-1}, where n = 1, 2, 3,.... The contours are overlaid on the SCUBA 850 μm image.

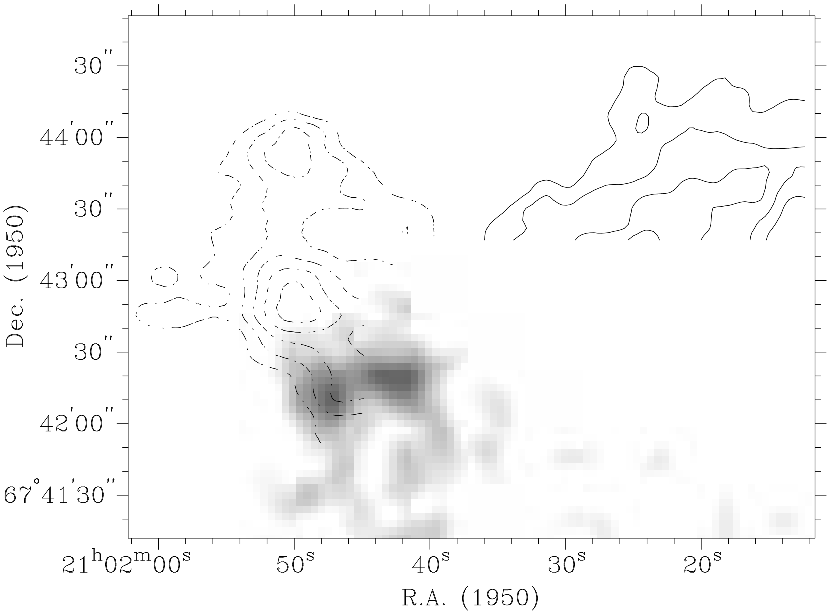

Fig. 26.— Partly mapped outflow in L1172. Redshifted gas is integrated over the range 4.0 to 10 km s^{-1} with contours at 8.0 + 2.0n K km s^{-1}, and blueshifted gas is integrated between -5.0 and 1.0 km s^{-1} with contours at 4.0 + 1.0n K km s^{-1}. The contours are overlaid on the SCUBA 850 μm image.

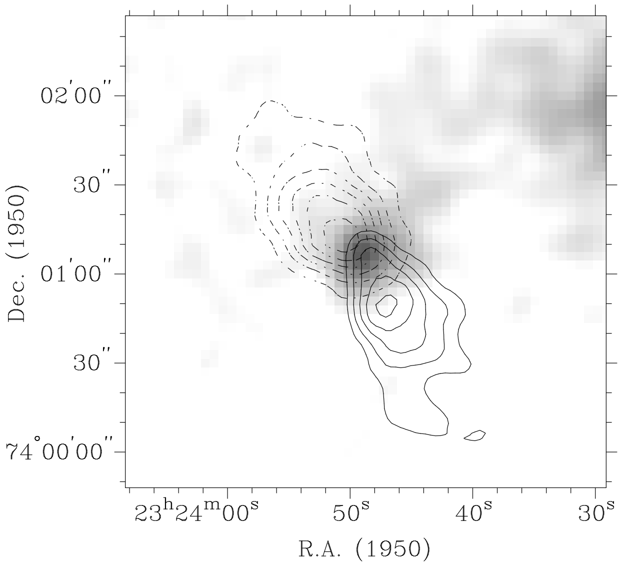

Fig. 27.— Outflow in L1262. Redshifted gas is integrated over the range 6.0 to 10.5 km s^{-1} with contours at 1.0 + 1.0n K km s^{-1}, and the blueshifted gas is integrated from -3.0 to 2.0 km s^{-1} with contours at 0.5 + 0.5n K km s^{-1}. The contours are overlaid on the SCUBA 850 μm image.

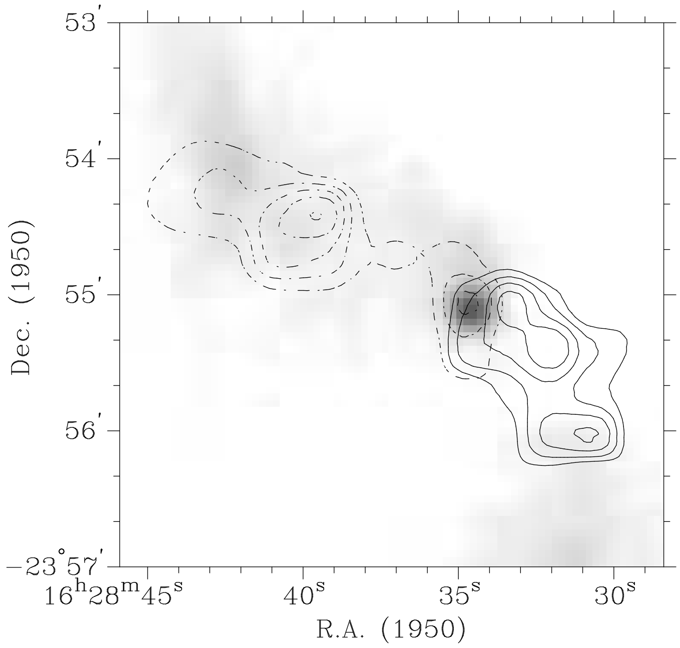

Fig. 28.— Outflow from L1709−SMM1 with redshifted gas integrated over the range 4.0 to 9.0 km s^{-1} and contours at 0.3 + 0.2n K km s^{-1}, and blueshifted gas integrated from -2.0 to 1.0 km s^{-1} with contours at 0.8 + 0.2n K km s^{-1}. The contours are overlaid on the SCUBA 850 μm image.

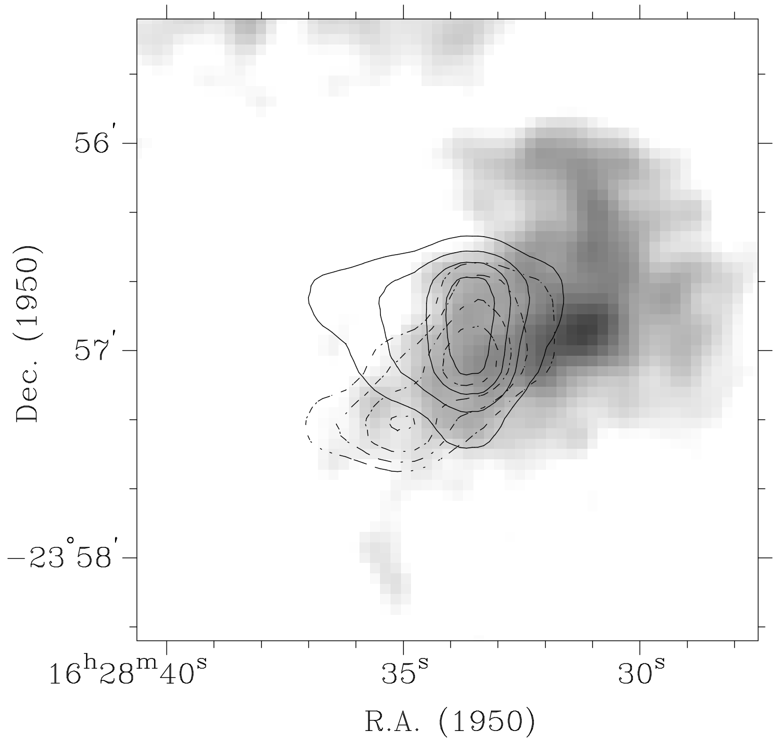

Fig. 29.— Outflow from L1709−SMM5 with redshifted gas integrated over the LSR velocity range 4.0 to 9.0 km s^{-1} and contours of $\int T_A^* dV$ at 1.0 + 1.0n K km s^{-1}, where n = 1, 2, 3,..., and blueshifted gas integrated from −2.0 to 1.0 km s^{-1} with contours at 3.2 + 1.5n K km s^{-1}. The contours are overlaid on a gray scale of the SCUBA 850 μm image.

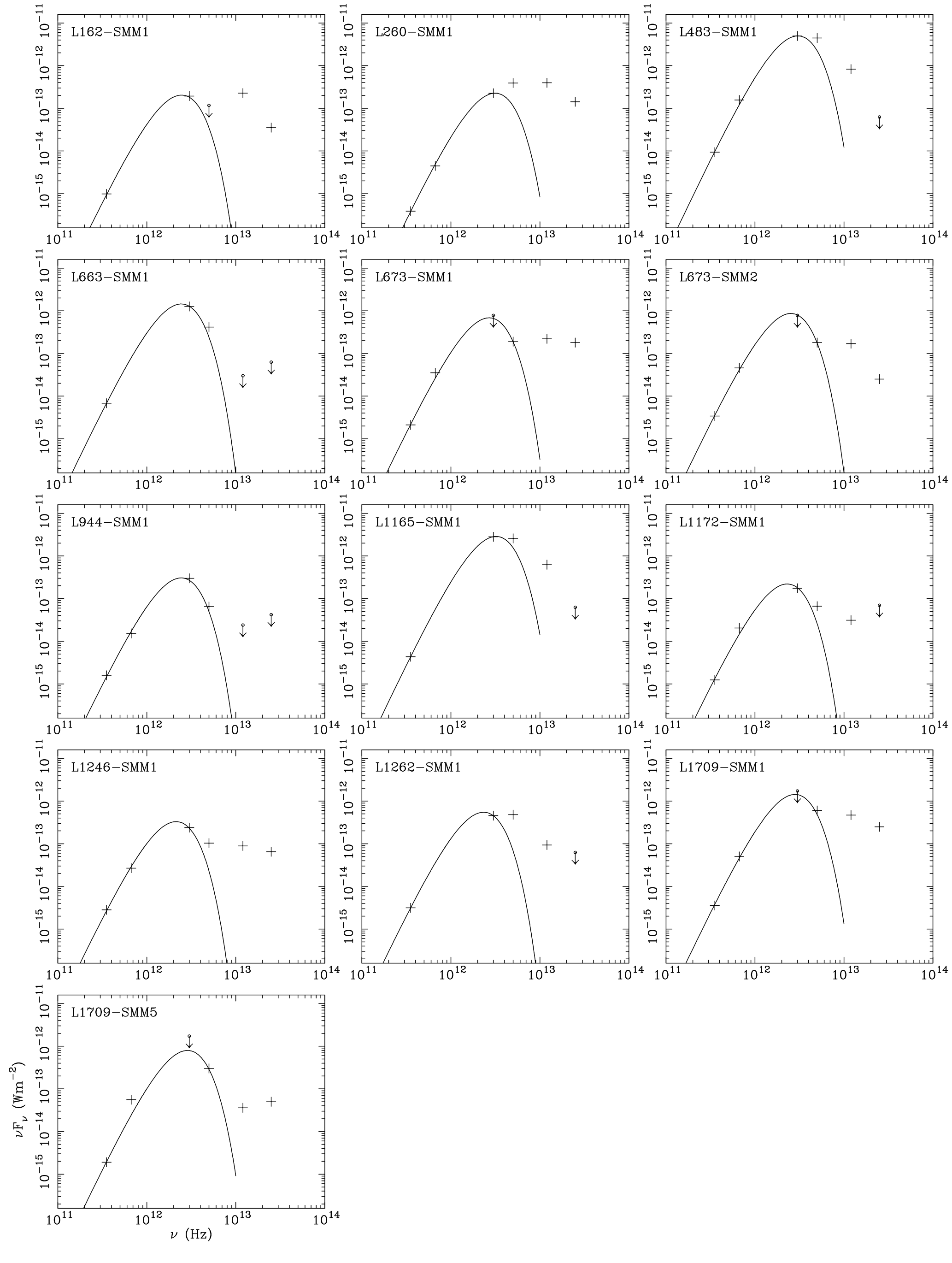

Fig. 30.— SEDs of all the protostars in the survey. The lines are gray-body fits to the submillimeter and far-infrared data, as described in the text.

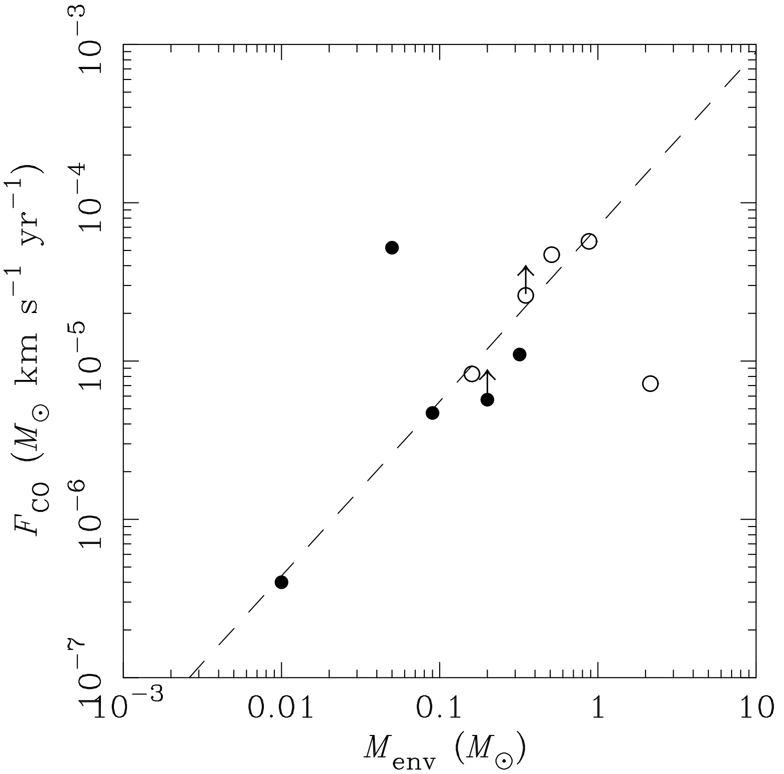

Fig. 31.— Outflow momentum flux (Table 5) vs. envelope mass. Open circles are the Class 0 sources, filled circles are Class I sources. The dashed line is the best fit found by Bontemps et al. (1996).

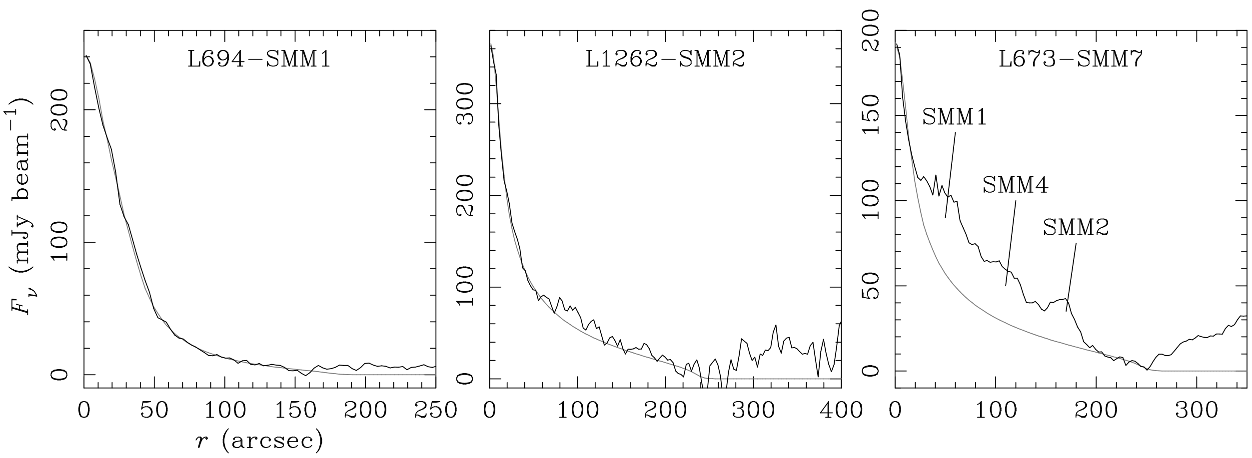

Fig. 32.— The 850 μm intensity profiles of three starless cores overlaid with best-fit isothermal models (*gray lines*). The three have been chosen to illustrate a good fit, L694−SMM1 (*left*), an average fit, L1262−SMM2 (*center*), and a very poor fit where adjacent cores can be seen in the radial profile, L673−SMM7 (*right*).

Table 1. The sample of Lynds opacity class 6 clouds.

Source	α(B1950.0)[a]	δ(B1950.0)[a]	Other Names[b]	$V_{\rm LSR}$ (km s^{-1})	D (pc)	References	Associated complex
L31	16 47 31	−19 02 15	CB67	4.8	160	1,2	Ophiuchus
L53	17 20 26	−23 59 45	···	?	160	···	Ophiuchus
L55	17 19 55	−23 54 30	B69	4.6	160	···	Ophiuchus
L57	17 19 36	−23 47 15	B68, CB82	3.5	160	2,3	Ophiuchus
L63	16 47 14	−17 59 00	···	5.8	160	1,3	Ophiuchus
L129	16 52 15	−16 17 15	···	?	160	1	Ophiuchus
L158	16 44 30	−13 52 45	···	4.3	160	1,3	Ophiuchus
L162	16 46 13	−14 05 30	···	?	160	1,3	Ophiuchus
L222	17 38 24	−19 46 00	CB94	10.6	160	···	Ophiuchus
L223	17 37 53	−19 42 00	CB93	10.3	160	···	Ophiuchus
L226	17 37 45	−19 38 00	CB92	10.5	160	2	Ophiuchus
L229	17 37 26	−19 31 15	···	?	160	···	Ophiuchus
L231	17 37 31	−19 32 45	···	?	160	···	Ophiuchus
L233	17 42 18	−20 00 00	B83A, CB95	11.1	160	2	Ophiuchus
L255	16 45 02	−09 49 30	···	?	160	1,3	Ophiuchus
L260	16 44 33	−09 31 45	···	3.5	160	1,3	Ophiuchus
L328	18 14 05	−18 03 00	B93, CB131	6.6	190	2,4	···
L483	18 14 56	−04 41 00	···	5.0	200	3,5	Aquila Rift
L543	19 04 11	−06 18 15	B134, CB181	11.3	400	3,6	···
L663	19 34 32	+07 27 30	B335, CB199	8.3	250	3,7	···
L673	19 18 25	+11 07 45	···	5.0	300	3,5	Cloud B
L675	19 21 31	+11 01 45	CB193	7.5	300	5	Cloud B
L694	19 38 45	+10 47 45	B143, CB200	9.6	250	7	···
L709	19 11 39	+16 21 45	CB184	6.3	300	2,5	Cloud B
L771	19 18 43	+23 24 15	CB190	11.0	400	5	Vul Rift
L860	20 01 26	+35 53 15	B146	?	700	8	Cygnus Rift
L917	20 38 11	+43 58 00	···	?	700	8,9	Cygnus Rift
L944	21 15 48	+43 05 30	···	5.5	700	8	Cygnus Rift
L951	21 18 20	+43 18 45	···	5.2	700	8	Cygnus Rift
L953	21 19 32	+43 08 15	···	6.3	700	8	Cygnus Rift
L1014	21 22 18	+49 46 30	···	4.7	200	3,10	···
L1021	21 19 58	+50 44 30	···	?	200	4	···
L1103	21 40 34	+56 30 00	···	?	150	3,6	···
L1111	21 38 54	+57 34 30	B161, CB233	−0.9	150	6	···
L1165	22 05 17	+58 52 15	···	−1.1	300	9	Cloud 157
L1166	22 03 47	+59 19 00	B173, CB236	−2.9	300	9	···
L1172	21 01 19	+67 33 15	···	4.5	440	3,11	Cepheus
L1185	22 27 34	+58 54 00	···	?	300	11	···
L1246	23 23 00	+63 20 00	CB243	−11.1	730	2,11	Cepheus OB3
L1262	23 24 19	+74 01 45	CB244	3.9	200	2,3,11	···
L1704	16 27 50	−23 35 30	CB65	2.4	160	···	Ophiuchus
L1709	16 29 36	−23 47 15	···	2.5	160	3	Ophiuchus

Note. — Units of right ascension are hours, minutes, and seconds, and units of declination are degrees, arcminutes, and arcseconds.

[a]Positions are from Parker (1988).

[b]B denotes the Barnard (1927) catalog, and CB denotes the Clemens & Barvainis (1988) catalog.

References. — (1) Nozawa et al. 1991; (2) Launhardt & Henning 1997; (3) Hilton & Lahulla 1995; (4) Lee & Myers 1999; (5) Dame et al. 1987; (6) Leung, Kutner, & Mead 1982; (7) Tomita, Saito, & Ohtani 1979; (8) Dame & Thaddeus 1985; (9) Dobashi et al. 1994; (10) Robert & Pagani 1993; (11) Yonekura et al. 1997.

Table 2. *IRAS* PSC associations with the Lynds dark clouds.

Source (1)	*IRAS* Name(s) (2)	F_ν(12 μm)[a] (Jy) (3)	F_ν(25 μm)[a] (Jy) (4)	F_ν(60 μm)[a] (Jy) (5)	F_ν(100 μm)[a] (Jy) (6)	Identification (7)
L53	17205−2359	.26L	.48L	.70L	12.23	···
L158	16442−1351	.31L	.52L	1.70	33.80L	···
	16445−1352	.27L	.33L	2.22	32.62	cirrus
	16439−1353	.32L	.45L	.78	27.56L	···
L162	16455−1405[b,c]	.63	.90	1.23	13.29L	T Tauri
	16464−1407	.60L	.36L	.63	6.48	···
	16457−1409	.33L	.34L	2.33L	5.26	···
	16459−1411	1.41	1.90	2.33L	6.47	T Tauri
L226	17375−1936	.64	.40L	.55L	19.61L	···
L255	16451−0953	.25L	.32L	.60	12.88	···
L260	16446−0924	.32L	.92L	.40L	5.30	···
	16446−0925	.25L	.69L	.40L	6.30	···
	16442−0930[c]	.57	3.31	7.83	7.54	protostar
	16450−0926[d]	.25L	.34L	.36	6.02	···
L483	18148−0440[c]	.25L	6.91	89.05	165.50	protostar
L663	19343+0727	.32	.25L	.40L	2.77L	···
	19345+0727	.25L	.25L	8.30	41.96	protostar
L673	19180+1116	1.09	2.22	3.51L	87.21L	···
	19180+1114	.41L	1.60	2.55L	105.70L	protostar
	19181+1056[c]	1.71	2.81	3.69	87.16L	T Tauri
	19181+1112	.38L	.43	5.59L	106.70L	···
	19181+1059	3.74	3.55	5.18L	91.15L	···
	19183+1123[d]	.96	.50	5.53L	82.50L	···
	19184+1055	3.74	5.46	3.69L	9.69	OH/IR star
	19184+1118	2.95	1.07	5.45L	71.62L	···
	19190+1105[b]	1.32	1.01	24.52L	86.05L	···
L694	19389+1048	.25L	.25L	.40L	7.91	···
	19380+1045	.54	.20	.40L	12.91L	···
L709	19116+1623	.97	.57	.98L	8.93L	···
L771	19186+2325[d]	.25L	.25L	1.03	6.61	···
L951	21186+4320	.25L	.25L	1.84L	6.84	···
L1165	22051+5849	2.16	.48	.53L	105.90L	···
	22051+5848[c]	.25L	5.22	51.59	94.00	protostar
L1172	21017+6742[d]	.28L	.26	1.33	5.83	protostar
L1246	23228+6320[c]	.26	.74	2.06	7.98	protostar
L1262	23238+7401[c]	.25L	.78	9.60	15.20	protostar
L1704	16277−2332[d]	.74L	.54L	.92	20.02L	···
L1709	16291−2351	.25L	.39L	.86L	3.59	···
	16285−2355[c]	1.19	3.73	9.44	60.86L	protostar
	16285−2356	.31L	.42L	1.01L	60.86	···
	16285−2358	.35L	.81	.97L	60.86L	star

[a] Flux density in the *IRAS* bands. "L" indicates an upper limit.

[b] *IRAS* source not covered by our SCUBA map.

[c] Source studied by Parker 1991.

[d] *IRAS* source not associated with the cloud by Parker 1988.

Table 3. Flux densities and cloud properties of the sample.

Source	Peak F_ν (Jy beam^{-1})[a] 450 μm	850 μm	Integrated F_ν (Jy) 450 μm	850 μm	Obs. Mode	Peak Mass ($M_\odot$)	Peak $N(\mathrm{H_2})$ ($\times 10^{26}$ m^{-2})	Peak $n(\mathrm{H_2})$ ($\times 10^{11}$ m^{-3})	Peak A_V (mag)	Total Mass ($M_\odot$)	Mean $N(\mathrm{H_2}) \times 10^{25}$ m^{-2}
L31	···	0.11±0.02	···	4.6	jiggle	0.06	1.5	3.9	15	2.2	5.5
L53	···	<0.12	···	···	jiggle	<0.05	<1.5	<4.0	<16	···	···
L55	···	0.10±0.02	···	1.1	jiggle	0.05	1.3	3.6	14	0.5	4.7
L57	1.1±0.19	0.14±0.02	45	2.8	scan	0.07	1.8	4.9	19	1.4	1.6
L63	2.6±0.23	0.31±0.03	945	52.3	scan	0.15	4.1	11.1	43	25.4	6.3
L129	···	<0.09	···	···	scan	<0.05	<1.3	<3.6	<14	···	···
L158	1.9±0.42	0.22±0.03	415	19.6	scan	0.11	3.0	8.0	31	9.5	2.2
L162	···	0.38±0.05	···	51.9	scan	0.18	5.1	13.7	53	25.2	4.2
L222	···	0.12±0.02	···	0.3	jiggle	0.06	1.5	4.1	16	0.2	5.5
L223	···	0.12±0.02	···	0.4	jiggle	0.06	1.5	4.1	16	0.2	5.8
L226	···	<0.09	···	···	jiggle	<0.05	<1.3	<3.5	<13	···	···
L229	···	<0.09	···	···	jiggle	<0.04	<1.1	<3.0	<12	···	···
L231	···	<0.09	···	···	jiggle	<0.04	<1.0	<2.8	<11	···	···
L233	···	<0.06	···	···	jiggle	<0.03	<0.9	<2.5	<10	···	···
L255	···	<0.09	···	···	scan	<0.04	<1.0	<2.8	<11	···	···
L260	1.4±0.24	0.21±0.02	16	1.1	scan	0.10	2.8	7.6	30	0.5	0.7
L328	0.7±0.12	0.21±0.02	8	1.7	jiggle	0.14	2.8	6.4	30	1.2	10.8
L483	6.5±0.23	1.30±0.03	400	13.1	scan	0.99	17.3	37.2	182	10.0	1.0
L543	···	<0.12	···	···	scan	<0.33	<1.4	<1.6	<15	···	···
L663	···	1.16±0.10	···	7.3	scan	1.38	15.4	26.6	162	8.7	20.9
L673	1.5±0.21	0.42±0.03	55	51.1	scan	0.71	5.5	7.9	58	87.4	3.4
L675	···	0.07±0.02	···	0.1	jiggle	0.11	0.9	1.3	9	0.2	3.4
L694	1.0±0.18	0.27±0.03	430	21.9	scan	0.32	3.6	6.1	37	26.0	1.0
L709	···	0.06±0.01	···	0.6	jiggle	0.10	0.8	1.1	8	1.0	3.1
L771	1.5±0.25	0.14±0.02	105	9.4	scan	0.43	1.9	2.0	20	28.6	3.9
L860	···	0.09±0.01	···	1.0	jiggle	0.87	1.2	0.8	13	9.4	3.6
L917	···	0.09±0.02	···	1.1	jiggle	0.85	1.2	0.7	13	10.4	4.4
L944	0.8±0.12	0.21±0.02	5	1.4	jiggle	1.99	2.9	1.8	30	13.0	6.0
L951	···	0.07±0.02	···	0.5	jiggle	0.66	0.9	0.6	10	4.7	4.0
L953	···	0.06±0.02	···	0.2	jiggle	0.59	0.8	0.5	9	2.2	3.6
L1014	0.8±0.12	0.15±0.02	5	0.9	jiggle	0.11	1.9	4.2	20	0.7	6.0
L1021	···	0.09±0.03	···	0.7	jiggle	0.07	1.2	2.7	13	0.5	4.8
L1103	···	0.11±0.03	···	1.4	jiggle	0.05	1.4	4.1	15	0.6	5.6
L1111	···	0.10±0.03	···	0.7	jiggle	0.04	1.3	3.7	13	0.3	5.0
L1165	···	0.99±0.12	···	17.2	scan	1.69	13.1	18.9	138	29.4	25.1

Table 3—Continued

Source	Peak F_ν (Jy beam^{-1})[a] 450 μm	850 μm	Integrated F_ν (Jy) 450 μm	850 μm	Obs. Mode	Peak Mass ($M_\odot$)	Peak $N(\mathrm{H_2})$ ($\times 10^{26}$ m^{-2})	Peak $n(\mathrm{H_2})$ ($\times 10^{11}$ m^{-3})	Peak A_V (mag)	Total Mass ($M_\odot$)	Mean $N(\mathrm{H_2}) \times 10^{25}$ m^{-2}
L1166	···	0.10±0.02	···	0.7	jiggle	0.17	1.4	2.0	14	1.2	4.9
L1172	2.6±0.30	0.20±0.03	770	12.3	scan	0.75	2.7	2.6	28	45.2	1.7
L1185	···	0.09±0.02	···	0.9	jiggle	0.15	1.2	1.7	13	1.5	4.5
L1246	1.8±0.15	0.40±0.02	13	4.0	jiggle	4.07	5.4	3.2	56	40.1	8.9
L1262	···	0.69±0.06	···	10.5	scan	0.53	9.2	19.8	97	8.0	14.8
L1704	0.8±0.19	0.10±0.02	···	0.5	scan	0.05	1.3	3.4	13	0.2	1.9
L1709	4.9±0.37	1.03±0.03	690	64.5	scan	0.50	13.7	36.8	144	31.4	8.4

[a]Uncertainties are statistical only; upper limits are 3σ.

Table 4. Submillimeter cores identified in the SCUBA maps.

Core	R.A. (B1950.0)	Decl. (B1950.0)	*IRAS* Association[a]	Searched for Outflow?	Outflow Detected?	Identification
L55−SMM1	17 19 55.3	−23 55 30	···	Yes	No	Starless core
L57−SMM1	17 19 35.7	−23 47 08	···	No	···	Probably starless
L63−SMM1	16 47 20.1	−18 01 12	···	Yes	No	Starless core
L158−SMM1	16 44 33.9	−13 53 50	···	Yes	No	Starless core
L158−SMM2	16 44 23.4	−13 53 01	···	No	···	Probably starless
L162−SMM1	16 45 56.1	−14 11 25	16459−1411	No	···	Known T Tauri star
L260−SMM1	16 44 13.7	−09 29 58	16442−0930	Yes	Yes	Known protostar
L260−SMM2	16 44 24.6	−09 29 46	···	No	···	Probably starless
L328−SMM1	18 14 05.0	−18 03 12	···	Yes	No	Starless core
L483−SMM1	18 14 50.2	−04 40 48	18148−0440	No	Yes[b]	Known protostar
L663−SMM1	19 34 35.1	+07 27 20	19345+0727	Yes	Yes	Known protostar
L673−SMM1	19 18 04.0	+11 16 37	19180+1116?	Yes	Yes	New protostar
L673−SMM2	19 18 04.6	+11 14 23	19180+1114	Yes	Yes	Known protostar
L673−SMM3	19 18 26.6	+11 08 31	···	Yes	No	Candidate protostar
L673−SMM4	19 18 03.5	+11 18 54	···	Yes	No	Starless core
L673−SMM5	19 18 30.3	+11 08 03	···	Yes	No	Probably starless
L673−SMM6	19 18 26.8	+11 10 19	···	Yes	No	Starless core
L673−SMM7	19 18 01.9	+11 17 10	···	Yes	No	Starless core
L673−SMM8	19 18 41.2	+11 06 04	···	Yes	No	Starless core
L694−SMM1	19 38 42.2	+10 50 03	···	Yes	No	Starless core
L860−SMM1	20 01 25.9	+35 53 30	···	No	···	Probably starless
L860−SMM2	20 01 29.0	+35 52 57	···	No	···	Probably starless
L944−SMM1	21 15 51.2	+43 06 08	···	Yes	Yes	New protostar
L951−SMM1	21 18 20.0	+43 19 17	···	Yes	No	Starless core
L951−SMM2	21 18 22.9	+43 19 51	···	Yes	No	Starless core
L1014−SMM1	21 22 23.9	+49 46 06	···	Yes	No	Starless core
L1165−SMM1	22 05 09.7	+58 48 05	22051+5848	Yes	Yes	Known protostar
L1172−SMM1	21 01 42.5	+67 42 19	21017+6742	Yes	Yes	Known protostar
L1172−SMM2	21 01 47.1	+67 42 13	···	Yes	No	Starless core
L1172−SMM3	21 01 35.6	+67 39 14	···	No	···	Probably starless
L1246−SMM1	23 22 51.9	+63 20 10	23228+6320	Yes	Yes	Known protostar
L1246−SMM2	23 23 03.5	+63 20 16	···	Yes	No	Starless core
L1262−SMM1	23 23 48.8	+74 01 07	23238+7401	Yes	Yes	Known protostar
L1262−SMM2	23 23 28.7	+74 01 58	···	Yes	No	Starless core
L1704−SMM1	16 27 49.8	−23 35 42	···	No	···	Probably starless
L1709−SMM1	16 28 34.6	−23 55 06	16285−2355	Yes	Yes	Known protostar
L1709−SMM2	16 29 28.4	−23 49 34	···	Yes	No	Starless core
L1709−SMM3	16 28 42.3	−23 54 04	···	Yes	No	Starless core
L1709−SMM4	16 29 46.3	−23 46 19	···	No	···	Ridge, probably starless
L1709−SMM5	16 28 31.3	−23 56 55	16285−2356?	Yes	Yes	New protostar

[a]The two *IRAS* sources indicated with a question mark (?) lie within 40″ of the submillimeter cores.

[b]L483−SMM1 was not searched for high-velocity gas, but its outflow has been extensively studied by other authors (see § 6.2.2).

Table 5. Outflow properties.

Protostar	Mass ($M_\odot$)	Energy (J)	Extent (AU)	ΔV (km s^{-1})	τ_d (yr)	Momentum Flux ($M_\odot$ km s^{-1} yr^{-1})
L260−SMM1	0.0002	4.8×10^{32}	7200	5.5	0.6×10^{4}	0.4×10^{-6}
L663−SMM1	0.0062	$>1.2\times10^{35}$	>23750	23.0	$>0.5\times10^{4}$	$\sim4.7\times10^{-5}$
L673−SMM1[a]	0.0052	7.4×10^{34}	48000	7.0	3.3×10^{4}	5.7×10^{-6}
L673−SMM2[a]	0.0260	4.0×10^{35}	54000	7.0	3.7×10^{4}	2.6×10^{-5}
L944−SMM1	0.0590	6.4×10^{35}	76400	11.0	3.3×10^{4}	5.7×10^{-5}
L1165−SMM1	0.0134	8.2×10^{34}	48000	8.5	2.7×10^{4}	1.1×10^{-5}
L1246−SMM1	0.0190	5.9×10^{34}	58400	6.0	4.6×10^{4}	7.2×10^{-6}
L1262−SMM1	0.0039	2.9×10^{34}	26000	10.0	1.2×10^{4}	8.3×10^{-6}
L1709−SMM1	0.0032	5.0×10^{35}	40000	11.0	1.7×10^{4}	4.7×10^{-6}
L1709−SMM5	0.0171	1.5×10^{35}	21600	11.0	0.9×10^{4}	5.2×10^{-5}

[a]The outflow properties of both L673−SMM1 and L673−SMM2 are based only on the blueshifted gas.

Table 6. Properties of the protostars in the sample of Lynds dark clouds.

Protostar	F_ν (Jy) 450 μm	850 μm	$T_{\rm dust}$ (K)	$L_{\rm bol}$ ($L_\odot$)	$L_{\rm submm}$ ($L_\odot$)	$L_{\rm bol}/L_{\rm submm}$	$T_{\rm bol}$ (K)	$M_{\rm env}$ ($M_\odot$)	$M_{\rm env}/L_{\rm bol}$ ($M_\odot/L_\odot$)	Outflow Efficiency	Class
L162−SMM1	···	0.28	22	0.5	6×10^{-3}	82	120	0.03	0.07	···	II
L260−SMM1	0.67	0.11	28	0.6	3×10^{-3}	250	104	0.01	0.02	30	I
L483−SMM1	23.62	2.67	27	9.0	0.10	91	55	0.33	0.04	···	0
L663−SMM1	···	1.93	21	2.8	0.10	29	31	0.51	0.18	820	0
L673−SMM1	5.28	0.60	24	2.8	0.05	59	70	0.20	0.07	100	I[a]
L673−SMM2	6.88	0.97	22	2.8	0.07	38	49	0.35	0.12	450	0[a]
L944−SMM1	2.54	0.42	21	4.4	0.17	27	30	0.88	0.20	630	0[a]
L1165−SMM1	···	1.23	28	11.7	0.10	115	59	0.32	0.03	50	I
L1172−SMM1	3.08	0.35	20	1.8	0.06	32	62	0.31	0.17	···	0[a]
L1246−SMM1	4.00	0.78	19	8.0	0.31	26	62	2.15	0.27	40	0
L1262−SMM1	···	0.89	20	1.1	0.03	40	57	0.16	0.14	370	0
L1709−SMM1	7.55	1.01	26	1.8	0.02	66	67	0.09	0.06	130	I
L1709−SMM5	8.36	0.54	25	0.9	0.01	75	44	0.05	0.06	270	I[a]

[a]Classifications ascribed by this work, not based on near/mid-infrared data.

Table 7. IRAS flux densities derived from HIRES images for several protostars.

Protostar	*IRAS* association	$F_\nu(12\ \mu\mathrm{m})$ (Jy)	$F_\nu(25\ \mu\mathrm{m})$ (Jy)	$F_\nu(60\ \mu\mathrm{m})$ (Jy)	$F_\nu(100\ \mu\mathrm{m})$ (Jy)
L673−SMM1	19180+1116	1.0	3.9	11.9	57.8L
L673−SMM2	19180+1114	0.2	0.3	6.0	57.8L
L944−SMM1	···	0.2L	0.2L	1.3	10.0
L1709−SMM1	16285−2355	0.7	1.8	3.8	26.1L
L1709−SMM5	16285−2356	0.1	1.4	3.5	26.1L

Table 8. Properties of the starless submillimeter cores.

Core	F_ν(850 μm) (Jy)	Aperture (arcsec)	Mass ($M_\odot$)	$N(\mathrm{H_2})$ ($\times 10^{25}$ m^{-2})	$n(\mathrm{H_2})$ ($\times 10^{10}$ m^{-3})	n_0 ($\times 10^{11}$ m^{-3})	r_0 (AU)	r_1 (AU)	γ	δ
L55–SMM1	0.34	80	0.16	2.5	1.3	0.20	8000	13000	1.3	2.0
L57–SMM1	1.43	200	0.67	1.7	0.3	0.47	6000	20000	0.7	1.6
L63–SMM1	1.31	140	0.61	3.1	0.9	1.55	4000	50000	0.7	1.8
L158–SMM1	1.02	180	0.48	1.5	0.3	0.20	25000	45000	0.9	2.0
L158–SMM2	0.19	60	0.09	2.4	1.7	...	...	...	...	...
L260–SMM2	2.10	200	0.99	2.4	0.5	0.22	13000	25000	1.0	2.0
L328–SMM1	0.84	90	0.56	4.8	1.9	1.72	3500	10000	0.6	2.1
L673–SMM3[a]	0.34	60	0.56	4.3	1.6	6.88	1500	47500	1.5	2.0
L673–SMM4	0.69	100	1.14	3.2	0.7	2.17	3500	67000	0.6	2.0
L673–SMM5	0.55	80	0.91	4.0	1.1	1.60	3900	29000	0.6	2.2
L673–SMM6	0.53	100	0.88	2.5	0.6	5.15	1000	60000	2.6	1.8
L673–SMM7	0.24	50	0.39	4.4	2.0	1.65	3000	75000	0.9	1.5
L673–SMM8	1.00	110	1.65	3.8	0.8	1.25	3500	33000	0.6	1.6
L694–SMM1	1.38	120	1.58	4.4	1.0	0.84	8000	45000	0.8	2.7
L860–SMM1	0.27	80	2.41	1.9	0.2	0.10	15000	40000	1.5	1.8
L860–SMM2	0.15	50	1.33	2.7	0.5	0.07	15000	37000	1.7	1.8
L951–SMM1	0.14	60	1.22	1.7	0.3	0.23	8000	20000	1.2	1.6
L951–SMM2	0.15	60	1.33	1.9	0.3	0.57	2000	80000	2.4	1.2
L1014–SMM1	0.55	90	0.40	3.1	1.2	0.71	4000	18000	1.4	1.8
L1172–SMM2	0.32	50	1.34	5.9	1.8	1.74	3500	40000	0.6	1.7
L1172–SMM3	1.30	180	4.61	1.8	0.2	0.07	50000	110000	0.9	1.7
L1246–SMM2	0.33	50	3.19	6.0	1.1	1.02	6000	33000	0.8	2.3
L1262–SMM2	1.31	100	0.96	6.0	2.0	12.40	1000	48000	0.9	1.5
L1704–SMM1	0.57	110	0.27	2.2	0.8	0.46	5000	16000	0.9	2.1
L1709–SMM2	1.42	120	0.67	4.5	1.6	2.47	3500	40000	0.7	1.8
L1709–SMM3	1.55	120	0.73	5.0	1.7	3.76	2000	45000	0.7	1.4
L1709–SMM4	2.51	180	1.18	3.6	0.8	...	...	...	...	...

[a]L673–SMM3 is a candidate protostar (see § 6.2.4).